Journal of Natural Gas Science and Engineering 36 (2016) 875–892

Contents lists available at ScienceDirect

Journal of Natural Gas Science and Engineering

journal homepage: www.elsevier.com/locate/jngse

Integrated simulation of multi-stage hydraulic fracturing in unconventional reservoirs

Huiying Tang [a, *], Philip H. Winterfeld [b], Yu-Shu Wu [b], Zhao-qin Huang [c], Yuan Di [a], Zhengfu Pan [d], Juncheng Zhang [d]

[a] College of Engineering, Peking University, Beijing 100871, People's Republic of China
[b] Department of Petroleum Engineering, Colorado School of Mines, Golden 80401, CO, USA
[c] School of Petroleum Engineering, China University of Petroleum, East China, Qingdao 266580, People's Republic of China
[d] CNPC CHUANQING Drilling Engineering Company Limited, People's Republic of China

ARTICLE INFO

Article history:
Received 10 September 2016
Received in revised form
28 October 2016
Accepted 4 November 2016
Available online 5 November 2016

Keywords:
Hydraulic fracturing
Thermal-hydro-mechanical coupling
Proppant transport
Wellbore modeling
DDM

ABSTRACT

In recent years, the multi-stage hydraulic fracturing technology has been widely applied to unconventional reservoirs. In order to optimize the stimulation performance and achieve economic production rates, the underlying physics and the impacts of different designing parameters must be quantitatively understood prior to the operations. Although many numerical models have been developed for this purpose, few are capable of properly taking into account the interplay of different mechanisms, such as fluid flow in the horizontal wells, fracture propagation, and proppant transport.

A novel 3D thermal-hydro-mechanical model entitled UFrac is developed in this paper. This model integrates the various mechanisms to capture the interactions among wellbores, fractures and reservoir rocks. The fluid flow inside the wells and the fractures is simulated with the finite volume method (FVM), the elastic deformations of rock mass are calculated with the 3D displacement discontinuity method (DDM), and fracture propagation is simulated with the fixed grid method. The UFrac model is capable of simulating the combined effects of multiple fracturing operation parameters, elastic interaction between fractures, and temperature redistribution induced by flow exchange.

By using the UFrac model, we investigate several key problems in hydraulic fracturing such as fracture height growth, perforation spacing optimization, and thermal effect on proppant placement. Important conclusions are drawn from the simulation results. The strength of stress interaction is found to be related to the fracture geometries. Stress shadow effect does not only affect the flow partitioning and fracture size distribution, but also influence the proppant transport. Friction loss in the wellbore can affect the decisions on spacing optimization. Moving inner fractures closer to the heel of the wells would be beneficial for fracture propagation balancing. Fluid viscosity loss due to heating from the surrounding formations results in longer but narrower fractures and faster settling of proppant. The modeling of proppant distribution aids in better characterization of the fracture conductivity, thus provides more reliable prediction of the well productivity.

1. Introduction

Multi-stage hydraulic fracturing has become a common practice for unconventional reservoir development. Despite the large amount of early production compared with non-fractured reservoirs, the production rate declines rapidly (Valkó and Lee, 2010), and about one third of the clusters are ineffective and do not contribute to gas production (Miller et al., 2011). The ability of hydraulic fractured wells to maintain economic production rates is of essential importance for production efficiency. The effectiveness of hydraulic fracturing is determined by many factors, such as rock properties, in-situ stress states, and operation parameters. Meanwhile, Hydraulic fracturing is a highly coupled process where wells, fractures, and reservoir rocks interact with each other in thermal-hydro-mechanical fashion. Thus, an integrated model which couples these core components is required to properly evaluate the role of each component in fracturing and to optimize future

* Corresponding author.
E-mail address: tanghuiying@pku.edu.cn (H. Tang).

http://dx.doi.org/10.1016/j.jngse.2016.11.018
1875-5100/

stimulation plans.

Numerous two dimensional hydraulic fracturing models have been built to investigate problems such as perforation optimization (Cheng, 2012a, b; Wu and Olson, 2015), interaction between hydraulic fractures and pre-existing weak planes (Cohen et al., 2013; Fu et al., 2013; Taleghani and Dahi Taleghani, 2009) and non-planar fracture propagations (Behnia et al., 2015). In spite of the importance of 2D models in revealing the basic physics in hydraulic fracturing, 2D representation of the fractures has severe limitations in modeling fracture height growth and proppant transport. These drawbacks can be partially compensated by some Pesudo-3D (Economides and Nolte, 2000; Valkó and Economides, 1995) and simplified proppant settlement (Weng et al., 2011) models. However, a 3D model is desired to provide more reliable and accurate predictions. For example, methods such as extended finite element method (Gupta and Duarte, 2014; Haddad et al., 2016) and phase field propagation model (Heister et al., 2015) have recently been proposed to extend the simulation into the third dimension. In this paper, the 3D displacement discontinuity method (DDM) which is an indirect boundary element method (BEM) is used to calculate the rock deformations in the multiple fracture system. First proposed by Crouch (1976), DDM has been widely used in fracture mechanics problems like fault deformation (Ritz et al., 2012), dike propagation (Maccaferri et al., 2011) and hydraulic fracturing (Bunger et al., 2012; Lecampion and Desroches, 2015; Maerten et al., 2014; McClure and Horne, 2014; Sesetty and Ghassemi, 2015; Zhang et al., 2009). The use of DDM creates some limitations for the model since formation rock is assumed to be homogeneous and linearly elastic. Although there are some restrictions, DDM allows the stress calculations to be carried out in two dimensional surfaces, which avoids mesh refining around the fractures. In this way, the computing efficiency can be greatly improved, which implies its potential to deal with a large number of fractures.

While several numerical models capable of simulating 3D fracture propagation exist, few models couple the hydro-thermal-mechanical processes in the multi-stage fracturing simulation. The models mentioned above mainly focused on mechanical part and the discussions of thermal effect are rare in the literature. Fracturing fluid properties are functions of temperature (Reyes et al., 2014), and these properties, such as fluid viscosity, are critical for successful fracturing treatment by influencing the hydraulic fracture geometry, proppant transport, proppant settling, fluid friction pressure loss, and fluid leakoff. Ribeiro and Sharma (2013) investigated the impact of temperature changes on energized fluid properties using the finite element method. Cohen et al. (2013) incorporated the thermal part into their unconventional fracture model and analyzed the relations between hydraulic fracturing and production. However, the simulations of fracture propagation and proppant transport were simplified to be pseudo-3D in Cohen's model, which may deliver results deviating from the more realistic full 3D models. In addition, only a few models (Lecampion and Desroches, 2015; McClure et al., 2015) have implemented the wellbore and proppant components in simulation and the influences of these two factors on multiple fracture propagation have not been investigated in detail. According to Cipolla et al. (2009), the proppant distribution had a significant effect on well productivity and to know the behavior of proppants was critical for production optimization. Thus, a numerical model which systematically integrates the wellbore, fracture, and proppant components could provide the insights on how to improve the effectiveness of hydraulic fracturing.

In this paper, a novel 3D thermal-hydro-mechanical model, referred to as UFrac, is presented. The fluid flow inside wells and fractures is simulated with the finite volume method (FVM), the elastic deformation of rock mass is calculated with the 3D displacement discontinuity method (DDM), and fracture propagation is simulated using the fixed grid model. The UFrac model is capable of simulating the combined effects of fracturing operation parameters, elastic interactions between hydraulic fractures, and temperature redistribution within wellbore and fractures.

The paper is organized as follows. First, we systematically introduce the governing equations of each mechanism and the underlying assumptions in UFrac. Second, the coupling procedure used in the model is presented. Then, the model results are validated against analytical and numerical solutions in literature. After validating the method, three sets of cases are designed to investigate problems like fracture height controls, simultaneous fracture propagation, and thermal effects. Finally, several conclusions based on the results are provided.

2. Methodology

Several important assumptions are made in the proposed model. We assume the in-situ stress state is in a normal faulting regime where the vertical stress is the maximum principle stress. The horizontal wells are assumed to have been drilled along the direction of minimum horizontal stress so that transverse hydraulic fractures will be generated. The curving of the fracture surface is not allowed at current model. Hydraulic fractures are assumed to be fully filled with fluid, so that no fluid lag exists between fracture front and fluid front. Under the high confining stress in typical shale reservoirs, fluid lag will vanish quickly based on the asymptote solution analysis (Lecampion and Desroches, 2015).

The model consists of two major parts: the wellbore and the fractures. High pressure fracturing fluid is pumped into a selected section of the wellbore, and the well pressure increases due to the compression from continuous fluid injection. Hydraulic fractures initiate under this high pressure and extend into the intact reservoir rock. The wellbore and fracture parts are fully coupled to build an integrated numerical frame to simulate the fracturing process. The program structure will be given at the end of section 2.

Similar with Adachi et al. (2007), hydraulic fracturing fluid, or slurry, is treated as a mixture of interpenetrating fluid and solid components. The fluid components consist mostly of water with some additives, such as gels, surfactants, crosslinkers, friction reducers, and breakers that affect fluid rheology. These fluid additives have a variety of purposes such as inhibitors, acids, biocides, and corrosion inhibitors. The solid components, called proppants, are added to stop the newly formed fractures from closing. Proppant size is assumed to be small enough compared to the fracture width so that proppant distribution can be described by volume fraction. When fracture width approaches proppant size, a block function is used to avoid nonphysical proppant transport.

2.1. Fluid characterization

The slurry density ρ_{sl} is the sum of the solid and fluid components:

$$\rho_{sl} = \sum_p c_p \rho_p + \left(1 - \sum_p c_p\right) \sum_f x_f \rho_f \tag{1}$$

where subscript p refers to the proppant component type and subscript f refers to the fluid component. The terms c_p and ρ_p are volume fraction and density of proppant p, and ρ_f and x_f are density and volume fraction of fluid component f in fluid phase respectively. Each proppant component, under the assumption of rigid body, is of constant density and the fluid component is assumed to

be slightly compressible.

$$\rho_f = \rho_{0,f}\left(1 + C_f\left(P - P_{ref}\right)\right) \tag{2}$$

where $\rho_{0,f}$ is fluid component's density at reference pressure P_{ref} and C_f is fluid component's compressibility. Slurry viscosity has contributions from both fluid and proppant components. Several expressions exist in the literature for the viscosity of suspensions containing solid particles (Nicodemo et al., 1974) and a general exponential relation is adopted:

$$\mu_{sl} = \mu_{fl}\left(1 - \frac{\sum_p c_p}{c_{max}}\right)^{-n} \tag{3}$$

where μ_{sl} and μ_{fl} are viscosities of the slurry and fluid portion respectively, c_{max} is the maximum proppant volume fraction at which slurry is essentially a solid, porous medium, and n is an exponent typically between 1.0 and 2.5. Note that this correlation can be problematic when the value of c_p is close to c_{max}. Pure fluid should still be able to flow through the "packed" proppants, but the mobility would be zeros in Eq. (3), which implies an infinitely large viscosity. If this scenario, a maximum allowable proppant concentration equals to $0.95c_{max}$ is chosen. Once proppant volume fraction reaches this value, no addition of concentration is allowed and the fluid behavior would be similar with flowing in a porous media with constant permeability. The viscosity of the fluid phase is computed with Grunberg and Nissan (1949)'s equation as:

$$\mu_{fl} = \sum_f \mu_f^{xf} \tag{4}$$

2.2. Wellbore modeling

The fluid flow in the wellbore is solved in UFrac with the finite difference method. The horizontal well is assumed to be consist of a series of connected linear well segments, each of which has a starting and ending measured depth (MD) and true vertical depth, and constant outer and inner radii. Slurry segments flow through the well in a piston-like manner and the fluid components of the slurry are assumed to be slightly compressible. Each component within one slurry segment has the same velocity. Fig. 1 shows a schematic of a wellbore model. There are both, a vertical one and a horizontal well segments, and three slurry segments in this example.

The mass balance equations for fluid flow within the wellbore of each slurry segment are:

$$\frac{\partial}{\partial t}\int_{S_{i+1}}^{S_i} \rho_{sl,i} A dS - \sum_j^{N_i} T_{wf,j}\rho_{sl,i}\left(P_{wi,j} - P_{f,j}\right) + \delta_{ij} q_{inj}\rho_{sl,0}$$

$$-\int_{S_{i+1}}^{S_i} T_{wr,i}\rho_{sl,i}(P_{wi} - P_{res})dS = 0 \tag{5}$$

where S_i and S_{i+1} are the starting and ending measured depths of slurry segment i, $\rho_{sl,i}$ is the average slurry density along segment i, and $\rho_{sl,0}$ is the slurry density at surface. The term N_i is the number of the initiated fractures within segment i, $P_{wi,j}$ and $P_{f,j}$ are well pressure and fracture pressure at the inlet of fracture j, q_{inj} is the injection rate of current segment which is non-zero only when segment i is currently under injection, $T_{wf,j}$ is the transmissibility between wellbore and connected fracture j (the expression for $T_{wf,j}$ will be given later), $T_{wr,i}$ is the flow transmissibility between wellbore and formation and P_{res} is the reservoir pore pressure which is assume to be constant. The unknowns in Eq. (5) include the location (S) and pressure (P_w) of each slurry segment. To close the equation system, an extra equation is required. The pressure gradient along the wellbore is caused by the gravitational and fractional effects:

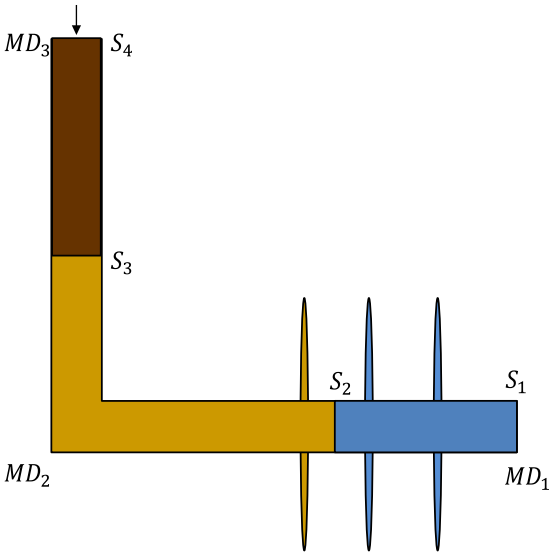

Fig. 1. Schematic of a wellbore with two segments and three stages. MD is the measured depth of each slurry segment. S denotes the fluid front of each injection segment. The top arrow denotes injection from surface. The narrow ellipses represent hydraulic fractures connecting to the borehole.

$$\frac{\partial P}{\partial s} = \rho\bar{g}\cdot\hat{s} + \frac{\partial P_{fric}}{\partial s} \tag{6}$$

where $\hat{s}$ is the unit vector along the well direction and $\bar{g}$ is the acceleration of gravity. The frictional pressure gradient $\partial P_{fric}/\partial s$ can be expressed as:

$$\frac{\partial P_{fric}}{\partial s} = \frac{4f}{D}\rho v^2 \tag{7}$$

where D is the diameter of wellbore, v is fluid velocity and f is the friction factor which is dependent on wellbore geometry, roughness and fluid flow regimes. The Reynold's number Re, defined with the well diameter and averaged flow velocity along the wellbore, is used to identify the flow regimes. Note that only Newtonian fluid is discussed here and the friction factor of Non-Newtonian fluid will have different expressions (Valkó and Economides, 1995). For fluid flow in a fracturing well, there may exist three different flow regimes along the wellbore: the laminar flow regime, the partially-developed turbulent flow regime, and the fully-developed turbulent flow regime. The critical Reynold's number for the transition from laminar flow to turbulence happens in a rough wellbore is approximately 2000 according be the literature (Eckhardt et al., 2007). Thus, we assume that once the Reynold's number excesses 2000, the flow within the wellbore enters turbulent flow regime. For laminar flow, $f = 16/\mathrm{Re}$ according to the Hagen-Poiseuille equation. When turbulence has been developed, the Colebrook-White equation (Colebrook and White, 1937), which took into account the experimental results for the flow through both smooth and rough pipes in the turbulent regime, is adopted,

$$\frac{1}{\sqrt{f}} = -0.86 \log_{10}\left(\frac{\varepsilon}{3.7D_h} + \frac{2.51}{Re\sqrt{f}}\right) \tag{8}$$

where ε is the pipe roughness and D_h is the hydraulic diameter. Due to the implicit nature of Colebrook's equation, the friction factor needs to be solved iteratively. To simplify this calculation, an explicit approximation derived by Chen (1979) is used, which gives suitable accuracy without any iterations:

$$\frac{1}{\sqrt{f}} = -4 \log_{10}\left(\frac{\varepsilon}{3.7} - \frac{5.0452}{Re}\log_{10}\left[\frac{\varepsilon^{1.1098}}{2.8257} + \left(\frac{7.149}{Re}\right)^{0.8981}\right]\right) \tag{9}$$

A clear description of the partially turbulent flow is still unavailable in the literature. Thus, Colebrook's equation is adopted as an approximation. Given the fact that hydraulic fracturing fluid is slightly compressible, flow velocity along the wellbore is assumed to be equal to the surface injection rate except for the fractured zones where a significant amount of fluid diverts into hydraulic fractures.

2.3. Governing equations for hydraulic fracture growth

The hydraulic fracture is assumed to be planar and perpendicular to the minimum principal stress σ_h. The fracture surface is divided into a series of rectangular grids of size 2a × 2b (a and b are half element lengths in x_1 and x_2 directions as shown in Fig. 2). Each element has its local coordinate system with x_3 axis along the normal direction. Before hydraulic fracturing, all fracture grids are defined to be inactive with zero displacements. When the high velocity fluid is injected, the well pressure, calculated with equations in Section 2.2, will build up until fractures start to initiate from the well wall. The fracture grid connecting to the borehole, which is also the first grid being activated, is called the initiation element. As pumping continues, the hydraulically induced fracture will propagate further into intact reservoir rock to active more fracture elements.

2.3.1. Elasticity

Fracture deformations are calculated with the 3D displacement discontinuity method proposed by Okada (1985). It is based on the analytical, elastic solutions of the normal and shear displacements of a finite rectangular discontinuity in half-space. The general idea of DDM is to approximate the distribution of displacement discontinuities of a crack by discretizing it into elements. Knowing the analytical solution of stresses induced by one crack element, the numerical solution of the whole domain can be calculated by superposition. The unknown displacements are obtained by satisfying the boundary conditions on fracture surfaces. The poro-elastic effect can also be considered with DDM (Tao and Ghassemi, 2010). However, we do not include this mechanism in our model for the reason that the permeability of unconventional reservoir is extremely low, and thus only a small amount of fluid can leakoff into the formation, which will not affect stress distribution significantly especially within the short stimulation period. The displacements of each fracture element are defined in the local coordinate (Fig. 2) with x_3 axis along the normal displacement direction:

$$D_s(x_1, x_2, 0) = u_1\left(x_1, x_2, 0^-\right) - u_1\left(x_1, x_2, 0^+\right)$$

$$D_d(x_1, x_2, 0) = u_2\left(x_1, x_2, 0^-\right) - u_2\left(x_1, x_2, 0^+\right)$$

$$D_n(x_1, x_2, 0) = u_3\left(x_1, x_2, 0^-\right) - u_3\left(x_1, x_2, 0^+\right) \tag{10}$$

The fracture deformation induced normal stress σ_n, strike direction shear stress τ_s, and dip-direction shear stress τ_d, that are applied on fracture element i can be calculated with the following equations.

$$\tau_s^i = \sum_{j=1}^{N} A_{ss}^{ij} D_s^j + \sum_{j=1}^{N} A_{sd}^{ij} D_d^j + \sum_{j=1}^{N} A_{sn}^{ij} D_n^j$$

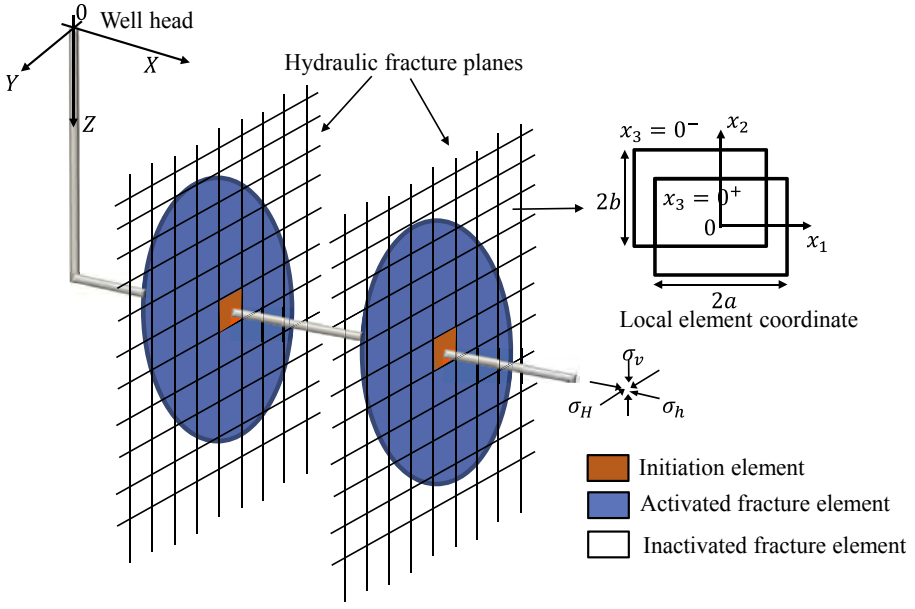

Fig. 2. Schematic of fracture propagation model used in this paper.

$$\tau_d^i = \sum_{j=1}^{N} A_{ds}^{ij} D_s^j + \sum_{j=1}^{N} A_{dd}^{ij} D_d^j + \sum_{j=1}^{N} A_{dn}^{ij} D_n^j$$

$$\sigma_n^i = \sum_{j=1}^{N} A_{ns}^{ij} D_s^j + \sum_{j=1}^{N} A_{nd}^{ij} D_d^j + \sum_{j=1}^{N} A_{nn}^{ij} D_n^j \tag{11}$$

where N is the total number of elements and A is the matrix of influence coefficients given by Okada (1985). For opened fractures, the total normal stress is equal to the fluid pressure and both strike and dip shear stresses are zero on no-slip fracture surfaces. Discussions of partially closed or cemented fractures following specific constitutive laws is not the focus of this paper and for readers who are interested, the work by McClure and Horne (2013) will provides some insights on this topic.

2.3.2. Fluid flow

The openings of fractures are functions of fluid pressure as discussed in section 2.3.1. To obtain the pressure distribution along fractures, a series of fluid flow equations are solved with finite volume method. Slurry equations are first solved to get the mixture velocity. A mass balance equation for each individual component is then solved to update the volume fractions. The general mass conservation equation and momentum equation of the multi-component slurry are given below:

$$\nabla\cdot(\rho_{sl}\vec{v}_{sl}w) + \frac{\partial}{\partial t}(\rho_{sl}w) + \dot{q}_{sl,wf}w - \dot{q}_{leak}\left(1-\sum_p c_p\right)\sum_f x_f\rho_f w = 0$$

$$\vec{v}_{sl} = -\frac{k}{\mu_{sl}}\nabla(p+\gamma z) \tag{12}$$

where ρ_{sl} is slurry density, $\vec{v}_{sl}$ is overall slurry velocity, w is fracture width, $\dot{q}_{leak}$ is the leakoff mass flow rate, and $\dot{q}_{sl,wf}$ is the mass exchange between borehole and fractures. p denotes fluid pressure, μ_{sl} is slurry viscosity and γ is the hydrostatic gradient. Since matrix permeability in unconventional reservoirs is extremely low, it would be difficult for solid components to flow into the matrix. Thus the leakoff of proppant is neglected. The fluid properties of the slurry are calculated with Eqs. (1)–(4). The permeability k can be calculated by assuming that the shape of fracture is a slit:

$$k = \frac{w^2}{12} \tag{13}$$

The one-dimensional Carter's leakoff model (Howard and Fast, 1957) is used to model fluid leakoff from fractures into the surrounding matrix,

$$\dot{q}_{leak} = \frac{C_{leak}}{\sqrt{t-\tau}} \tag{14}$$

where C_{leak} is the leakoff coefficient, τ is the time when fluid first arrives, and t is the current time. Fluid components are assumed to have the same velocity as the slurry, and the slip between proppant and carrying fluid is characterized by gravity induced settlement,

$$v_{fl,x} = v_{sl,x} \;;\; v_{p,x} = \chi v_{sl,x}$$

$$v_{fl,z} = v_{sl,z} \;;\; v_{p,z} = \chi\left(v_{sl,z} + v_{p,stl}\right) \tag{15}$$

where subscript x denotes the direction along fracture length, z denotes the direction parallel to the gravity acceleration vector g, fl represents fluid component, p is the proppant component, $v_{p,stl}$ is the settling velocity of proppant relative to slurry, and χ is the block function used to account for proppant bridging which will be introduced later. Friehauf (2009) presented expressions for proppant velocity in terms of slurry velocity and other variables. Correction factors were introduced that account for inertial effects, the effect of interfering proppant particles, and the effect of the fracture wall. The proppant settling velocity has the form:

$$v_{stl,z} = v_{stokes} f(N_{re}) g(c_p) h(w) \tag{16}$$

where v_{stokes} is the Stoke's settling velocity, $f(N_{re})$ captures inertial effects, $g(c_p)$ models the effect of interfering proppant particles, and $h(w)$ represents the effect of the fracture walls. These expressions are in the forms:

$$v_{stokes} = \frac{\left(\rho_p - \rho_f\right) g_{frac} d_p^2}{18\mu_{fl}}$$

$$f(N_{re}) = \frac{0.3736\mu_{fl}{}^{0.57}}{\rho_f^{0.29}\left(\rho_p-\rho_f\right)^{0.29} d_p^{0.86}}$$

$$g(c_p) = -5.9\left(\sum_p c_p\right)^3 + 8.8\left(\sum_p c_p\right)^2 - 4.8\left(\sum_p c_p\right) + 1$$

$$h(w) = 0.563\left(\frac{d_p}{w}\right)^2 - 1.563\left(\frac{d_p}{w}\right) + 1 \tag{17}$$

where d_p is proppant diameter and g_{frac} is the gravity constant projected on the fracture plane. The above expressions for proppant settling velocity are based on the assumption of spherical particle shape. If irregular or non-spherical proppants are to be considered, the applicability of Friehauf's model should be carefully validated.

A block function introduced by Shiozawa and McClure (2016) is used to capture proppant bridging (explained in section 4.2) when the fracture width is comparable to the proppant diameter.

$$\chi = \begin{cases} 1, & \text{if } w \geq N_{max}d_p \\ \dfrac{w - N_{min}d_p}{(N_{max}-N_{min})d_p}, & \text{if } N_{min}d_p \leq w < N_{max}d_p \\ 0, & \text{if } w < N_{min}d_p \end{cases} \tag{18}$$

Proppants can flow into or out of the fracture element only when fracture aperture is greater than N_{min} times the proppant diameter. The block function increases linearly from 0 to 1 when the ratio of fracture element width to proppant diameter changes from N_{min} to N_{max}. Without loss of generality, we choose N_{min} and N_{max} to be 2 and 3 respectively.

After calculating the velocities of fluid and solid components (Eq. (15)), the volume concentration of each component is calculated with mass conservation in the form of advective equations:

$$\nabla\cdot\left[\rho_f\vec{v}_{fl}x_f\left(1-\sum_p c_p\right)w\right] + \frac{\partial}{\partial t}\left[\rho_f x_f\left(1-\sum_p c_p\right)w\right] - \dot{q}_f = 0$$

$$\nabla\cdot\left[\vec{v}_p c_p w\right] + \frac{\partial}{\partial t}\left[c_p w\right] - \dot{q}_p = 0 \tag{19}$$

With the above equations, the fluid volume fraction x_f and proppant concentration c_p at the current time step can be solved.

Finally, by neglecting pressure loss due to perforation friction, the mass exchange between the wellbore and hydraulic fracture $\dot{q}_{sl,wf}$, is calculated according to Peaceman (1978)'s formulation of well index.

$$\dot{q}_{sl,wf} = \frac{T_{wf}\rho_{sl}\left(P_w - P_f\right)}{4ab} = \frac{WI\rho_{sl}}{4ab\cdot\mu_{sl}}\left(P_w - P_f\right)$$

$$WI = -\frac{2\pi k_f w}{\ln(r_w/r_o)}, \quad r_o = 0.14\sqrt{a^2+b^2} \tag{20}$$

where r_w is the well radius, a and b are the sizes of initiation fracture element (Fig. 2).

2.3.3. Fracture initiation and propagation

Assuming the formation rock is linear elastic and has a tensile failure strength T_0, the breakdown pressure $P_{b,w}$ for fracturing the surface of the borehole can be calculated with elasticity theory (Timoshenko and Goodier, 1951) to give:

$$P_{b,w} = 3\sigma_h - \sigma_H - P_p + T_0. \tag{21}$$

Strictly speaking, the above equation is only applicable to open hole completion and axial initiation of hydraulic fractures. However, even for horizontal wells where the eventual hydraulic fracture orients transversely to the well and perpendicular to minimum horizontal stress, axial initiation is still favorable (Abbas et al., 2013). Furthermore, this criterion just provides an approximation of the initial pressure in the initiation element (Fig. 2), which will not significantly affect the propagation process in later period.

A fixed grid fracture propagation model (Barree, 1983) is used in this paper. Instead of capturing fracture front with implicit level set functions (Peirce and Bunger, 2013), we use a simple correlation to calculate the fracture propagation distance according to the stress intensity factor at the current time step (Mastrojannis et al., 1979; Ribeiro and Sharma, 2013):

$$\Delta d = max\left\{\Delta d_{max}\left(\frac{K_I - K_{IC}}{K_I^{max} - K_{IC}}\right), 0\right\} \tag{22}$$

where Δd_{max} is the maximum propagation length, K_I is the type I stress intensity factor at the fracture tip, K_I^{max} is the maximum stress intensity factor along the front, and K_{IC} is fracture toughness of reservoir rock. Since the fracture is assumed to be planar, only the type I stress intensity factor is required. Once Δd is larger than the fracture element length, a newly opened element will be added at the front. Note that a large Δd_{max} implies fast propagation velocity. To fill the new element with fluid, however, a longer time is required compared to the situation when a small Δd_{max} is chosen. Thus the overall propagation velocity is similar with different choices of Δd_{max}. With DDM, the stress intensity factor K_I can be easily obtained with:

$$K_I = C\frac{D_n E\sqrt{\pi}}{4(1-\nu^2)\sqrt{d}} \tag{23}$$

where E is Young's modulus, ν is Poisson's ratio, d is the half length of fracture grid, D_n is the normal displacement of tip element, and C is an empirical constant to correct the DDM based stress intensity factor calculation. The correction factor 0.806 derived by Olson (1991) is used in this paper. Although this value is based on 2D analysis, it also gives good approximation in 3D problems (Sheibani, 2013).

2.4. Temperature modeling

UFrac also deals with temperature redistribution due to heat exchange between injection fluid and surrounding rocks. Reservoir rock is assumed to be of constant temperature and the thermal induced stress changes are not considered.

The energy conservation equation in the wellbore includes terms for energy accumulation, heat exchange between wellbore and fractures, heat injection from well head, and heat loss into surroundings through conduction:

$$\begin{aligned}&\frac{\partial}{\partial t}\int_{S_{i+1}}^{S_i}\rho_{sl,i}\overline{u}_{sl,i}AdS - \sum_j^{N_i} T_{wf,j}\rho_{sl,i}\left(P_{wi,j} - P_{f,j}\right)\overline{h}_{sl,i} + \delta_{ij}q_{inj}\rho_{sl,0}\overline{h}_{sl,0}\\ &- \int_{S_{i+1}}^{S_i} 2\pi r_w H(T - T_{res})dS\\ &= 0\end{aligned} \tag{24}$$

The same notation with Eq. (5) is used. $\overline{u}_{sl}$ and $\overline{h}_{sl}$ denote internal energy and enthalpy of slurry respectively, H is the heat transfer coefficient between the wellbore and surrounding formations, T is fluid temperature within the fracture, and T_{res} is temperature of contacting formation rock which is taken as a constant in the current model.

Energy balance equations in fractures are also expressed in terms of slurry as:

$$\begin{aligned}&\nabla\cdot\left(\rho_{sl}\overline{h}_{sl}\overrightarrow{v}_{sl}w\right) + \frac{\partial}{\partial t}\left(\rho_{sl}\overline{u}_{sl}w\right) - \dot{q}_{cond} - \dot{q}_{leak}\left(1 - \sum_p c_p\right)\\ &\times\sum_f x_{fl}\rho_{fl}\overline{h}_{fl}\\ &= 0\end{aligned} \tag{25}$$

where $\overline{h}_{sl}$ is the slurry enthalpy, $\overline{u}_{sl}$ is internal energy, $\dot{q}_{cond}$ is heat conduction from fracture surface to surrounding rock and fluid leak off rate, and $\dot{q}_{leak}$ is calculated with Eq. (14). Slurry enthalpy is defined as the combination of different components:

$$\rho_{sl}\overline{h}_{sl} = \sum_p c_p\rho_p\overline{h}_p + \left(1 - \sum_p c_p\right)\sum_f x_f\rho_f\overline{h}_f \tag{26}$$

Enthalpy and internal energy of each component is calculated as.

$$\overline{h}_x = \overline{u}_x = C_x(T - T_o),\ x = p, fl \tag{27}$$

where C_x is heat capacity of fluid and solid components and T_o is a reference temperature. The changes of enthalpy and internal energy are treated to be the same with the assumption of a constant pressure process. The heat loss $\dot{q}_{cond}$ from fracture surface in Eq. (25) is derived from one-dimensional heat conduction process,

$$\dot{q}_{cond} = 2\sqrt{\frac{K_{th,res}\rho_{res}C_{p,res}}{\pi(t-\tau)}}(T - T_{res}) \tag{28}$$

where subscript *res* refers to contacting reservoir, $K_{th,res}$ is thermal conductivity, ρ_{res} and $C_{p,res}$ are density and heat capacity of the reservoir (including rock and internal fluid).

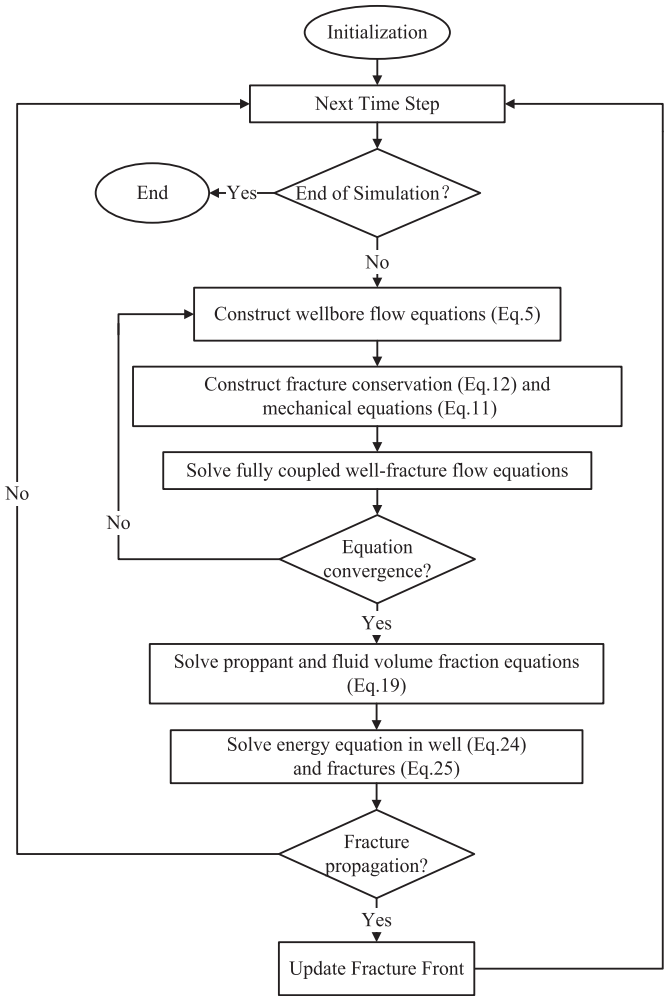

Fig. 3. Flow chart of iteration loop and coupling procedure.

2.5. Coupling procedure

The coupling procedure is illustrated as follows (Fig. 3): wellbore flow equation (Eq. (5)), fracture flow equation (Eq. (12)), and mechanical equation (Eq. (11)) are implicitly solved using Newton-Raphson iteration. The primary variables, well head pressure, slurry segments locations, fracture pressure and width, which strongly interact with each other, are solved in a fully coupled way. The flow equations for each component (Eq. (19)) and the energy equations (Eq. (25) and Eq. (26)) are iteratively solved to update fluid component volume fractions and temperature distribution at time step level. Constant and adaptive time stepping (Ribeiro, 2013) can both be applied in the model. Fracture propagation is checked at the end of each time step. The initial width of the newly added fracture element is set to be zero, which satisfies the mass balance condition.

3. Model validation

To validate the model results, comparisons have been made against both existing analytical solutions and with numerical solutions from published works. Subsection 3.1 validates the fracture deformation and induced stress calculated with DDM. In Subsection 3.2, the elastic stress interaction among multiple fractures is validated with other numerical work (Wu, 2014). Subsection 3.2 simulates the radial fracture propagation without fluid leakoff.

3.1. Mechanical calculation validation

In this part, the mechanical results based on 3D DDM is validated with analytical solution and existing numerical results.

For the case of uniformly pressurized radial fractures in a linear elastic material, fracture widths w along radius r and normal stress σ_n in the near tip region follow analytical solutions (Sneddon, 1946),

$$w = \frac{8p_o(1-\nu^2)}{\pi E}\left(c^2-r^2\right)^{1/2} \quad ; \quad \sigma_n = -\frac{2p_o}{\pi}\left(sin^{-1}\frac{1}{r} - \frac{1}{\sqrt{r^2-1}}\right) \tag{29}$$

where p_o is the fluid pressure, E is the Young's modulus, ν is the Poisson's ratio, and c is the fracture radius. The definition of r is shown in Fig. 4 (left). The fracture radius c is chosen to be 1 m, inner pressure equals to 10 Pa, Poisson's ratio and Young's modulus are 0.1 and 10^5 Pa respectively.

316 rectangular elements are used to approximate the radial shape of the fracture in this case. The comparisons between

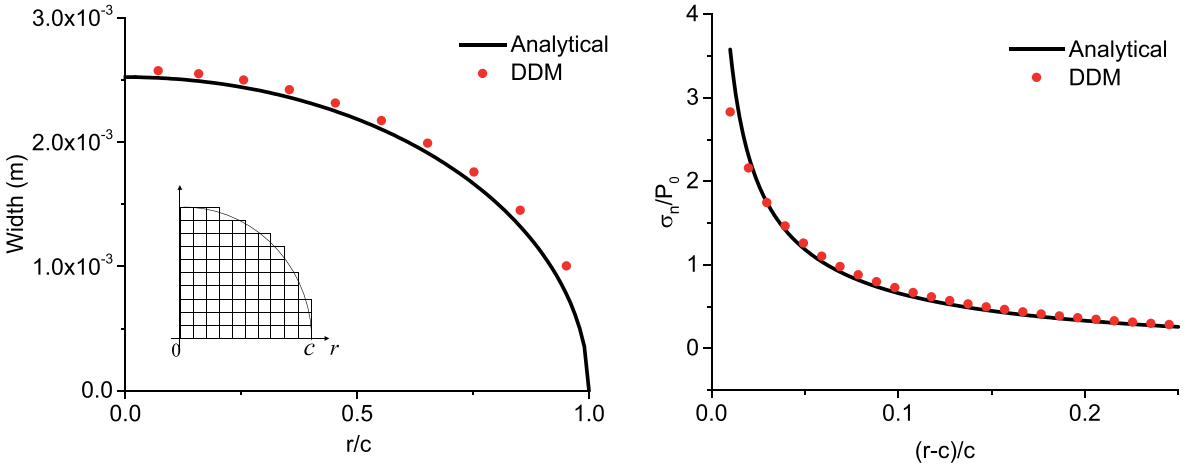

Fig. 4. Radial fracture width (left) and near tip normal stress (right) comparison between numerical results (UFrac) and analytical solutions.

Table 1
Input parameters used for three parallel fractures.

Parameter	Unit	Value
Fracture height	ft	100
Fracture length	ft	400
Young's modulus	psi ($\times 10^6$)	4
Poisson's ratio	–	0.25
Internal pressure	psi	5806
Minimum horizontal stress	psi	6096
Element number in x direction	–	40
Element number in z direction	–	10

(Geertsma and De Klerk, 1969):

$$R(t) = 0.56\left(\frac{Eq^3}{2\mu(1-\nu^2)}\right)^{1/9} t^{4/9} \tag{30}$$

where q is the volumetric injection rate, E is the Young's modulus, ν is the Poisson's ratio and μ is the fluid viscosity. The values used in the simulation are given in Table 1. The maximum propagation distance Δd_{max} is chosen to be 5 m in this case. Different Δd_{max} values have been tested, and the final results are not sensitive to the choice of Δd_{max}. Table 2 shows the values of the rest input parameters used in the simulation.

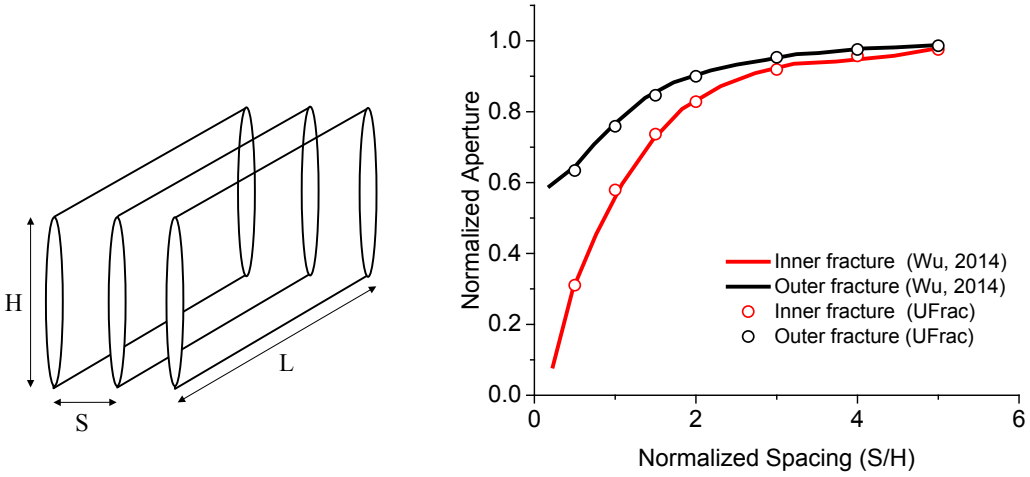

Fig. 5. Illustration of a three fracture system (left) and the stress shadow effect on the system (right). The normalized aperture is defined as the ratio of the fracture center aperture to an isolated single fracture aperture. S and H denotes the fracture spacing and height as depicted in this figure.

Table 2
Input parameters for radial fracture propagation validation.

Parameter	Unit	Value
Viscosity	cp	20
Injection rate	bbl/min	20
Young's modulus	psi ($\times 10^6$)	2.5
Poisson's ratio	–	0.25
Minimum horizontal stress	psi	5000
Fracture toughness	psi$\cdot\sqrt{\text{m}}$	145
Element size in x direction	m	1
Element size in z direction	m	1

analytical solutions and numerical results calculated with UFrac are given in Fig. 4. An excellent match of both fracture deformations and near tip stresses is observed.

To further verify the stress calculations in a multiple fracture system, a case of three parallel rectangular fractures is tested. The reference results, which are also calculated with DDM, are taken from Wu (2014). Model parameters are listed in Table 1. Due to the stress shadow effect, the inner fracture has smaller aperture compared with the outer fractures. As fracture spacing increases, the stress interaction between fractures vanishes and each fracture gradually deforms independently when spacing is over roughly 2.5 times longer than fracture height. Again, the results calculated by UFrac match very well with reference solutions (Fig. 5).

3.2. Radial fracture propagation

For the case when minimum horizontal stress is homogeneous along the vertical direction, radial fractures will be generated. The radius of the radial fractures without leakoff can be calculated as

Fig. 6 shows a match of the analytical solution and numerical results. The step-like shape of the numerical solution results from the fact that rectangular grids are used to approximate the fracture radial shape. In early time, the numerical model gives higher propagation velocity because only a few grids are activated in the beginning and such a coarse grid will overestimate the stress intensity factor at the fracture tip. As a result, the model overestimates the velocity the fracture grows. As fracture propagation continues, more fracture elements are added, and the calculated

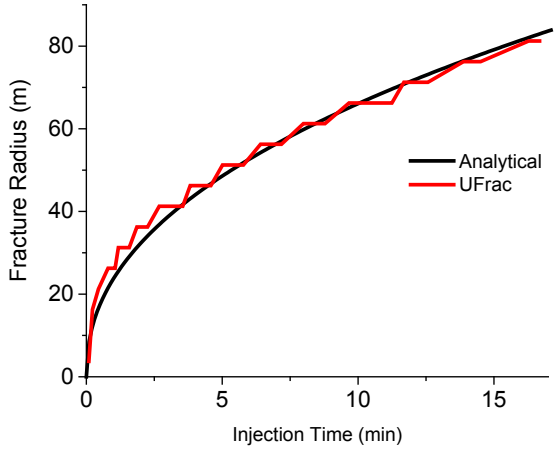

Fig. 6. Fracture radius calculated by numerical and analytical methods.

Table 3
Input parameters for case studies.

Parameter	Unit	Value
Viscosity (Base Fluid)	cp	1
Density (Base Fluid)	kg/m^3	1020
Injection rate	bbl/min	20
Injection time	min	2.2
Young's modulus	psi ($\times 10^6$)	2.5
Poisson's ratio	–	0.25
Fracture toughness	psi$\cdot\sqrt{\text{m}}$	145
Element size in x direction	m	3
Element size in z direction	m	2

stress intensity factor starts to stabilize and converge to the actual values. Thus, the numerical solution gradually matches the analytical solution as demonstrated in Fig. 6.

4. Application

In the previous sections, the details of the integrated hydraulic fracturing simulation model were introduced, and different aspects were verified. In the following section, a set of case studies will be conducted to illustrate the capability of this model to analyze and solve important problems encountered in unconventional reservoir stimulations. The implications and potential use of the simulation results are also discussed.

4.1. Fracture height growth in multi-layer formations

Fracture height growth and containment are not only important for operation effectiveness but also for environmental concerns (K. Fisher and Warpinski, 2012). According to the data provided in Fisher's paper (Fisher and Warpinski, (2012)), hydraulic fractures may propagate upward, downward or be well contained in the target zone depending on stress states, fault distributions and other reservoir properties.

In this paper, height growth of hydraulic fractures in layered formations is modeled with stress heterogeneity. We assume the propagating fracture will directly penetrate the layer contacts. For the case where step over or dilation happens, the contacting surfaces should be modeled explicitly with certain constitutive laws (Zhang et al., 2007). In this section, we study two situations: constant in-situ stress distribution along the vertical direction and heterogeneous vertical stresses. The parameters used in the simulations are given in Table 3.

With the assumption of homogeneous in-situ stress distribution, fracture geometry as well as proppant transport occurs in a radial pattern (Fig. 7, (a) (b)). Due to the existence of gravity, the fracture propagates downward further than upward (Fig. 8(a)). For the case of the heterogeneous stress distribution, the minimum horizontal stress at the injection layer is 30 MPa which is the same with the homogeneous case. The stress distribution along the vertical direction is depicted in Fig. 7. The upper layer and lower layer act as stress barriers with stresses 32 MPa and 31.5 MPa

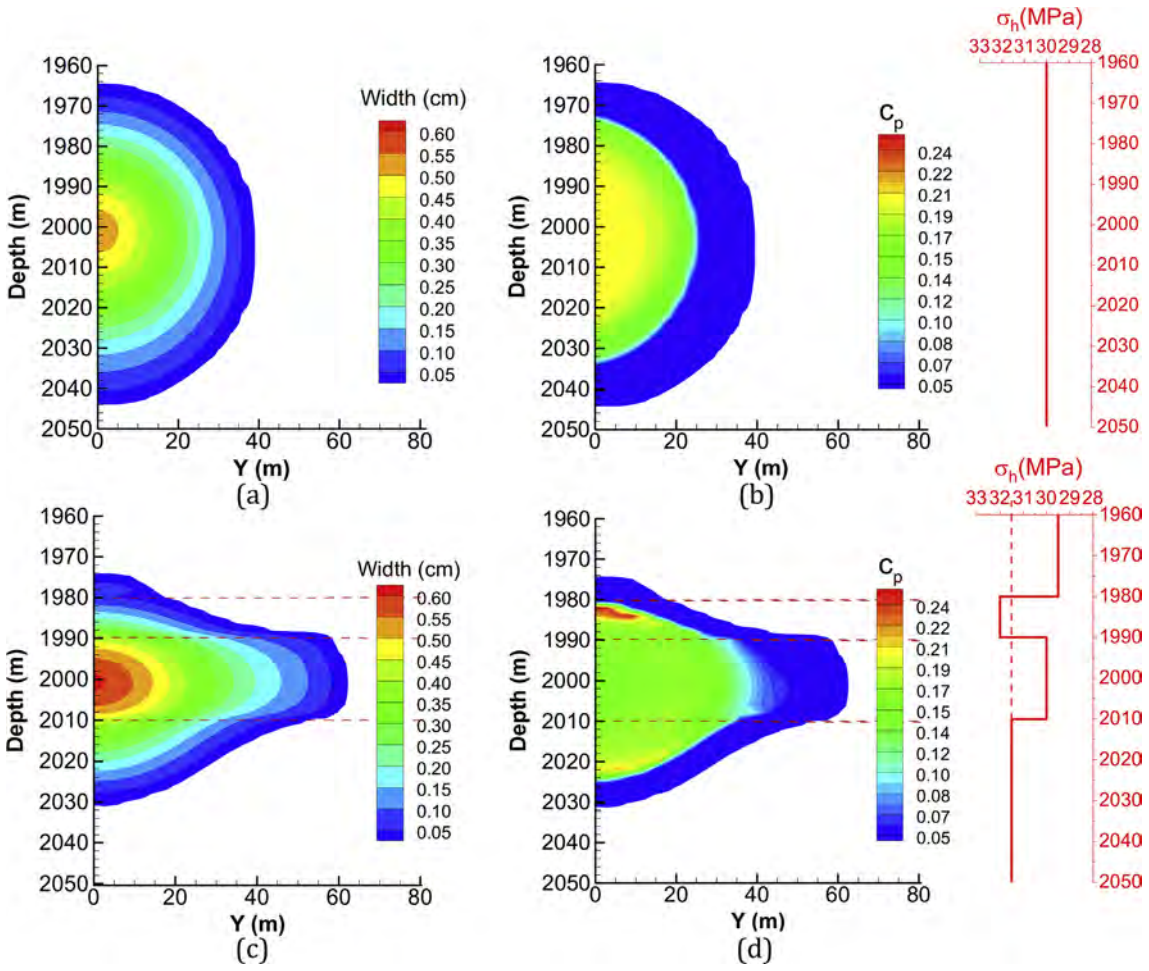

Fig. 7. Fracture width profile (a, c) and proppant volume fraction distribution (b, d) along horizontal direction with different minimum horizontal stress distributions.

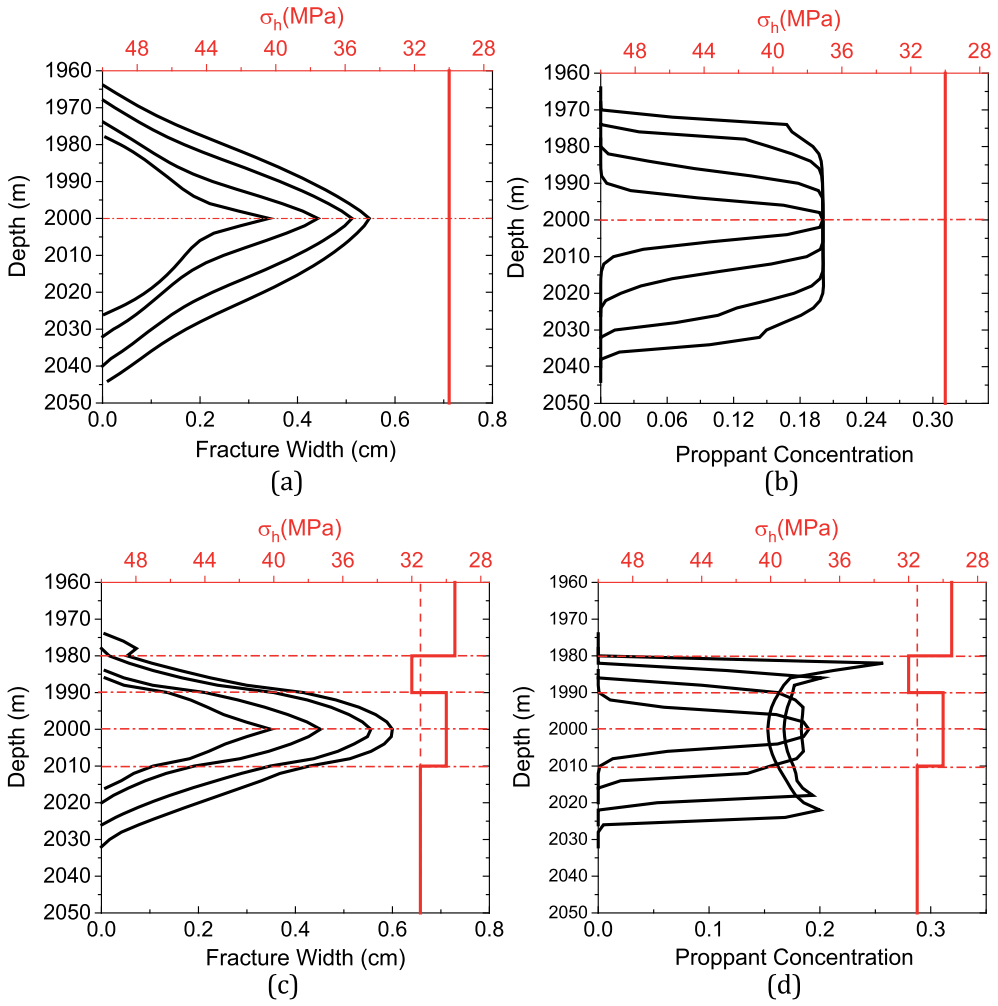

Fig. 8. Fracture width profile (a, b) and proppant volume fracture distribution (c, d) along the vertical direction at the injection point with different minimum horizontal stress distributions. The corresponding times for different profiles are 0.5 min, 1 min, 2 min and 3 min.

Table 4
Input parameters for case studies.

Parameter	Unit	Value
Horizontal well length	m	500
Well depth	m	2000
Well radius	cm	5
Welbore roughness	mm	1
Young's modulus	GPa	20
Poisson's ratio	–	0.25
Fracture toughness	MPa	1
Tensile strength	MPa	2
Minimum horizontal stress ($\sigma_{h,0}$)	MPa	30
Minimum horizontal stress in confining layer ($\sigma_{h,1}$)	MPa	33
Reservoir temperature	°C	80
Injection rate	bbl/min	20
Base fluid density	kg/m^3	1020
Gel density	kg/m^3	1020
Base fluid viscosity	cp	1
Gel viscosity	cp	20
Base fluid specific heat	J/kg	4184
Gel specific heat	J/kg	4184
Fracture-surrounding heat transfer coefficient	J/m^2-sec	20
Proppant diameter	mm	0.45
Proppant density	kg/m^3	2800

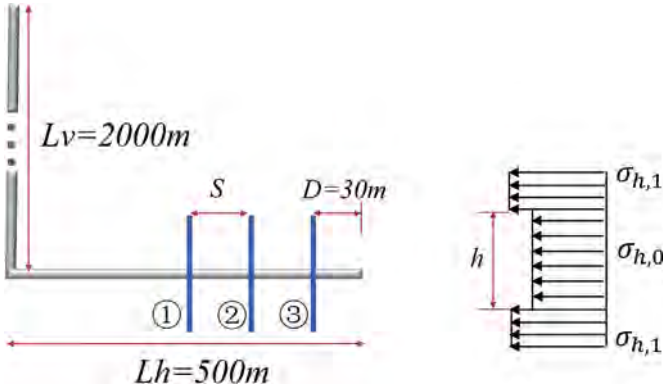

Fig. 9. Schematic of the wellbore and fracture configurations. Three fractures are simultaneously stimulated in the horizontal well segment. The numbering of fractures is 1, 2, 3 from heel to toe. Different sedimentary layers have different minimum horizontal stresses σ_h. Target zone is of height h.

respectively. When layered stress is applied on the fracture surface, the shape of fracture can no longer be described with simple geometry and the fracture tends to propagate in the layers that have smaller confining stresses (Fig. 7, (c) (d)). The stress containment in the vertical direction benefits fracture length growth in the horizontal direction, and the resulting fracture width is also larger

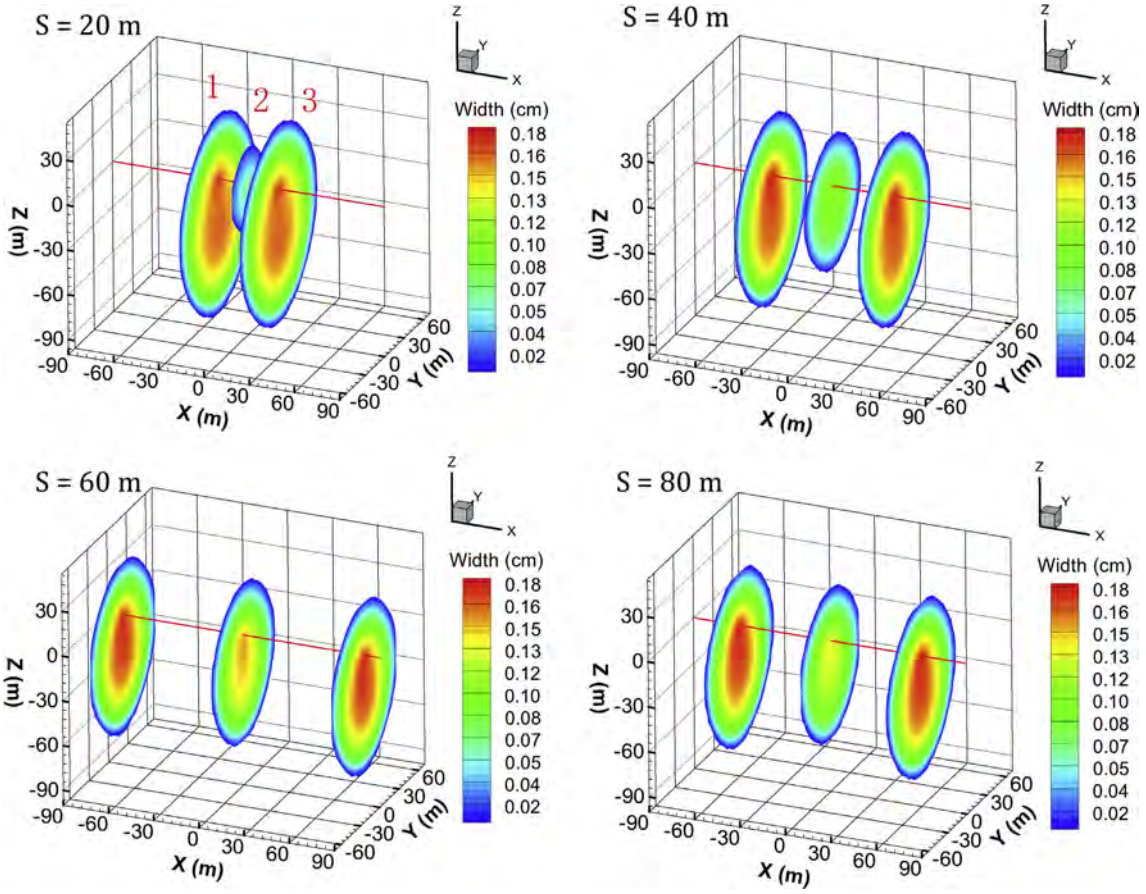

Fig. 10. Fracture geometry and width distribution of a simultaneously stimulated three fracture stage. Perforation spacing (S) changes from 20 m to 80 m.

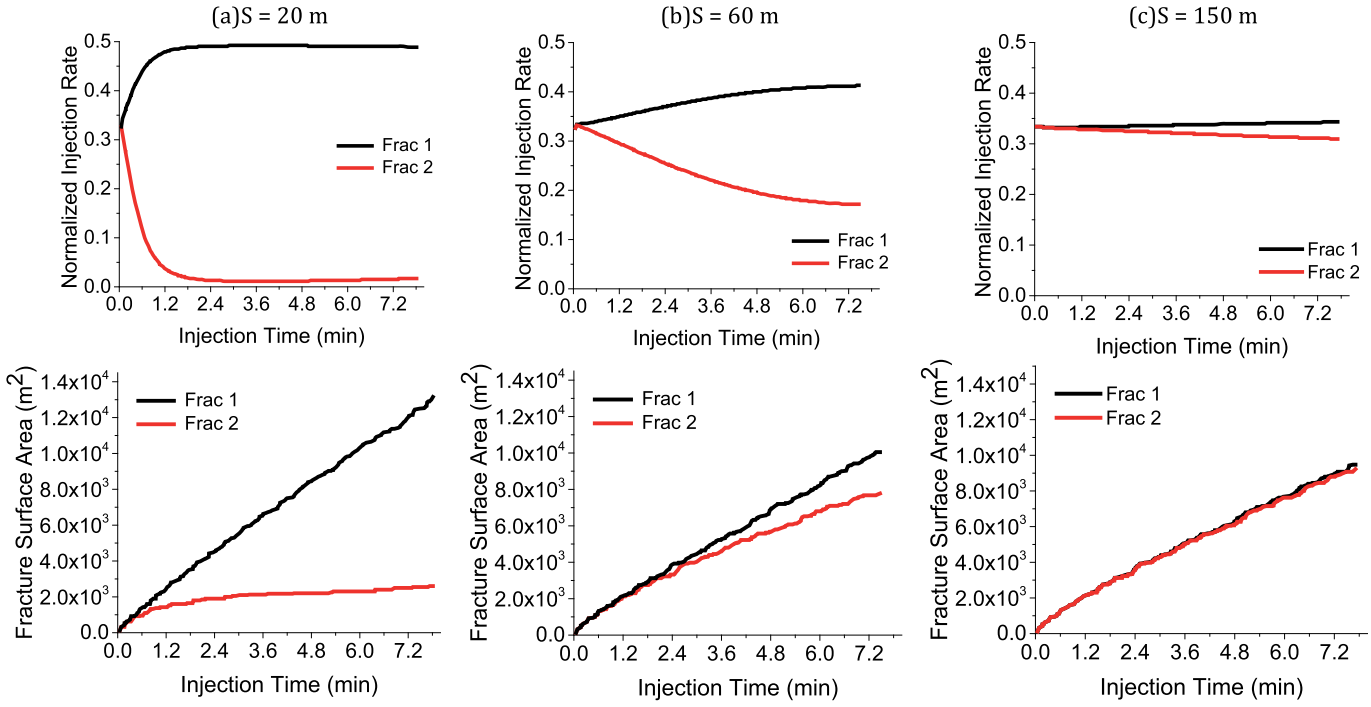

Fig. 11. Flow rate and fracture surface area (defined as the area of one face of fracture) comparison between inner and outer fractures with different fracture spacing.

than the homogeneous scenario (Fig. 8, (a) (c)). Since the lower layer has slightly smaller stress, it's easier for fractures to propagate into the lower formation. Meanwhile, after penetrating the upper layer, a less confined layer is encountered and the fracture width in this layer is recovered (Fig. 8(c)). The stress variation not only affects the shape of the fracture but also affect the proppant movement within fractures. An approximately homogeneous proppant distribution is observed in the case without stress barriers except for a slight proppant bridge built up at the last time step (3 min) (Fig. 8(b)). If the layered stress distribution exists, however, proppants tend to accumulate in high stress layers, and clear proppant bridges are formed (Fig. 7(d) and Figure 8(d)). Even though the fracture can cross through the barrier layers, no proppant can reach into these depths which means these parts of fractures will not contribute to production after fracture shut-ins.

As demonstrated in the above examples, assumptions like constant height or circular fracture shape can be easily violated given practical stress distributions. In-situ stress distribution plays a significant role in the determination of the final fracture profile and proppant placement.

4.2. Multi-stage hydraulic fracturing

One of the major concerns of hydraulic fracturing is the optimization of fracture spacing. If the fractures are too far away from each other, the total fracture surface area will not be enough to deliver economic production rate. However, if the fractures are too close, the elastic interaction between fractures, also called stress shadow effect, will restrict the fracture size and result in ineffectively stimulated fractures.

First we investigate the effects of perforation spacing on stimulation performance. Four cases, spacing with 20 m, 40 m, 60 m, and 80 m are modeled with consideration of gravity. In this case, well friction and fluid leakoff are ignored and fracture pressure at the injection point is set to be the same with well pressure. Model inputs are listed in Table 4. Model configurations, well geometry, parameter definitions, and fracture numbering are illustrated in Fig. 9.

Consider simultaneously fracturing of a three fracture stage in a horizontal well (Fig. 9). The vertical part of the well is 2000m and the horizontal portion is 500 m. Fractures are equally spaced with distance S. After injecting base fluid for 8 min, the final fracture

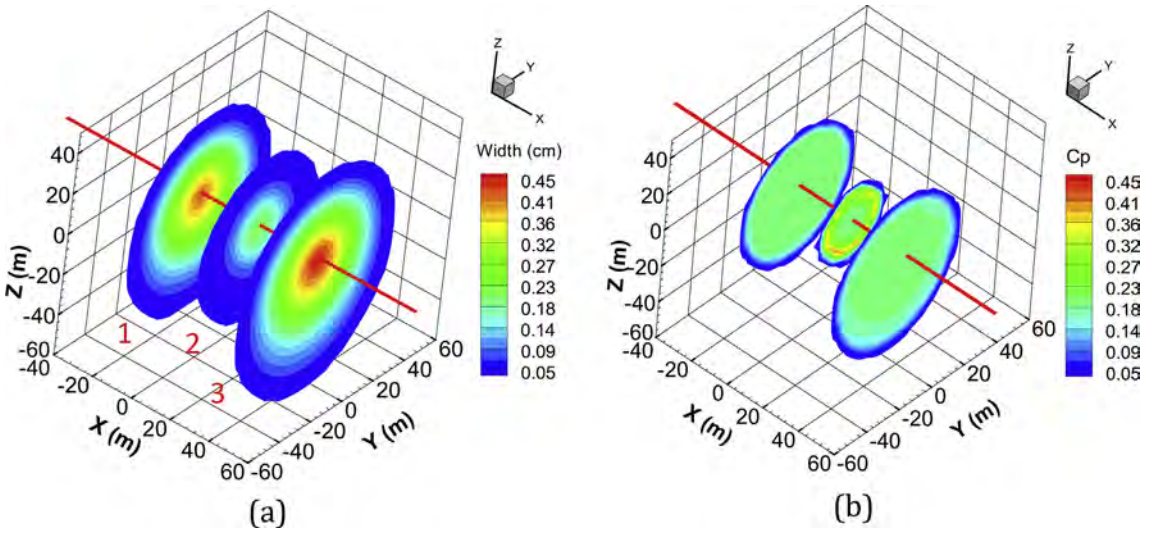

Fig. 12. (a) Fracture width distribution and (b) proppant volume fraction at the end of injection.

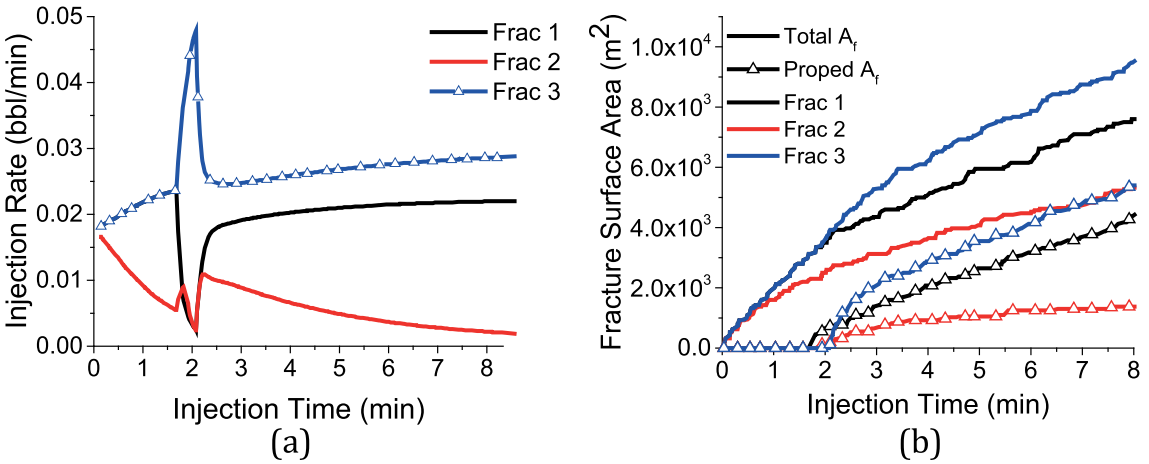

Fig. 13. (a) Injection rate of slurry from wellbore to each fracture. Fracture numbering is the same with Fig. 10. (b) Fracture surface area and propped fracture surface area comparison.

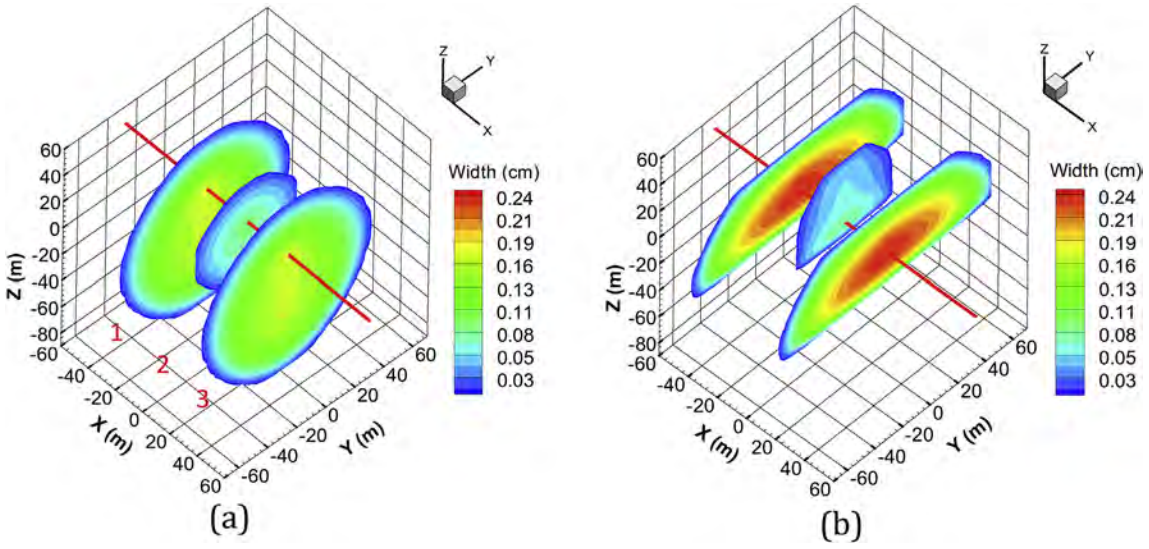

Fig. 14. Impact of fracture geometry on stress interactions. (a) Radial fractures developed in homogeneous in-situ stress condition. The red straight line represents horizontal well. (b) PKN shaped fractures resulting from stress confinement on adjacent layers. Fracture spacing is 30 m in both cases. (For interpretation of the references to colour in this figure legend, the reader is referred to the web version of this article.)

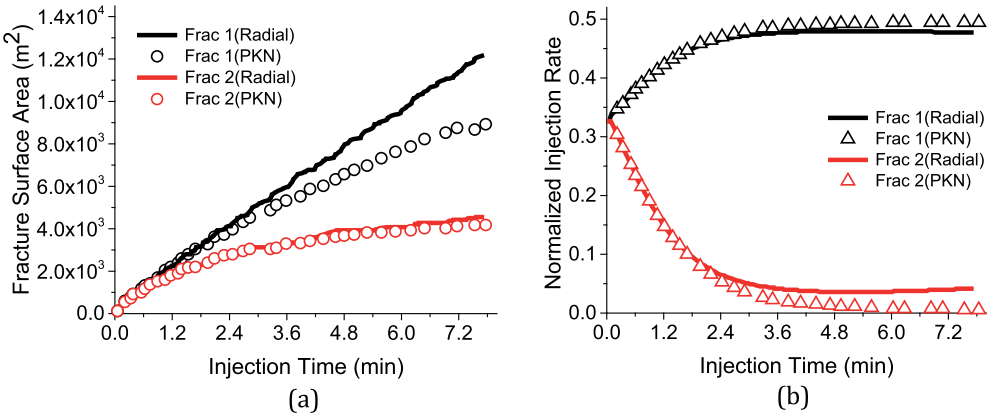

Fig. 15. Comparison of injection rate and fracture surface area in inner (Frac 2) and outer (Frac 1) fractures with different geometries.

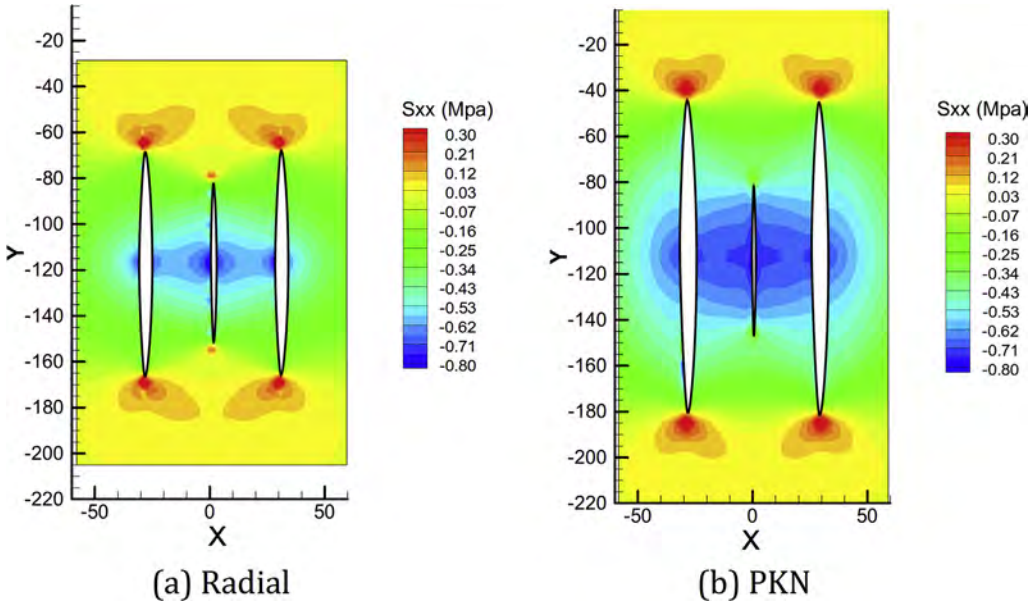

Fig. 16. Fracture deformation induced normal stress at perforation depth. (a) Radial geometry fractures (Fig. 13(a)); (b) PKN geometry fractures (Fig. 13(b)). Fracture width is enlarged proportionally for display purpose. Compressive stress is taken as negative in this figure.

geometry and width distribution are depicted in Fig. 10 with different fracture spacing, varying from 20 m to 80 m.

Both fracture surface area and width are affected by the distance between fracture perforations (Fig. 10). In early stage, when fractures are relatively small, interference among fractures is not profound. The growth of fractures will increase the deformation induced stresses which enlarge the difference of compression applied on outer and inner fractures. For the case of 20 m spacing, propagation of inner fracture is strongly suppressed by the outer fractures and almost no fluid can enter the inner fractures, especially at later stage (Fig. 11(a)). With increasing fracture spacing, flow rate is gradually balanced among fractures. In the meantime, the surface area of each fracture becomes similar (Fig. 11). A monotonic increase of difference among fractures is observed, which implies a time-dependent operation may optimize the stimulation effectiveness. In agreement with the conclusion drawn by previous studies (Cheng, 2012a, b), when fracture spacing is 2.5 times larger than fracture length (in the case 150 m spacing and 60 m fracture radius), the stress shadow effect vanishes and each fracture begins to be mechanically independent with few stress interactions (Fig. 11(c)).

Small spacing results in small width of the center fracture, which may also cause problems for proppant transport. Once the fracture width decreases to be comparable with proppant size, the movement of proppant is prohibited and a bridge between proppant laden fluid and pure fluid will be formed. This phenomenon is called proppant bridging. After injecting pure base fluid for 2 min, proppant with properties listed in Table 4 is injected with Gel. Well friction is ignored in this case and the inlet pressure is assumed to be the same among fractures.

When proppant transport is considered, proppant bridging close to the fracture tip is observed (Fig. 12(b)). Due to the compression from outer fractures, the propagation of the inner fracture is prohibited, which results in the accumulation of proppant at the fracture front. Moreover, the middle fracture with smaller aperture forms proppant bridges more easily than other fractures. The combined effect makes proppant movement in inner fractures quite difficult, and only a small portion of the fracture area can be effectively propped. It is clear from Fig. 13(b) that the unevenness of the propped fracture surface area is more severe than the total fracture area. Although the inner fracture keeps growing, the area that is effectively filled with proppant changes little. Since the unpropped part of fractures will be closed when pumping stops, and thus no longer contributes to production, it is important to add the proppant aspect into the model to better evaluate the effective fracture conductivities.

One can also observe from Fig. 12 and 13 that the symmetry between Frac 1 and Frac 3 (defined in Fig. 12(a)) doesn't hold when proppant is injected. Before proppant arrives to the current stage, the two outer fractures act the same (Fig. 13). When proppant reaches Frac 1, if the injection rate in each fracture is maintained, the resulting pressure built-up in Frac 1 will be higher than the fractures that haven't received proppant yet. Because well pressure is assumed to be the same within one stage, the injection rate of the fracture which first accepts proppant (in this case Frac 1) will decrease to maintain pressure equilibrium. As a result, other fractures will receive more fluid and the resulting uneven growth of outer fractures is observed (Fig. 12(a)). After proppant arrives at all fractures, flow partition is stabilized again and a new balance is reached (Fig. 13(a)).

The conclusions above are based on the assumption of homogeneous in-situ stress and only radial shaped fractures. As illustrated in the previous section, when the fracture is well confined in the target zone with overlying and underlying layers acting as stress containments, Perkins-Kern-Nordgren (PKN) shaped

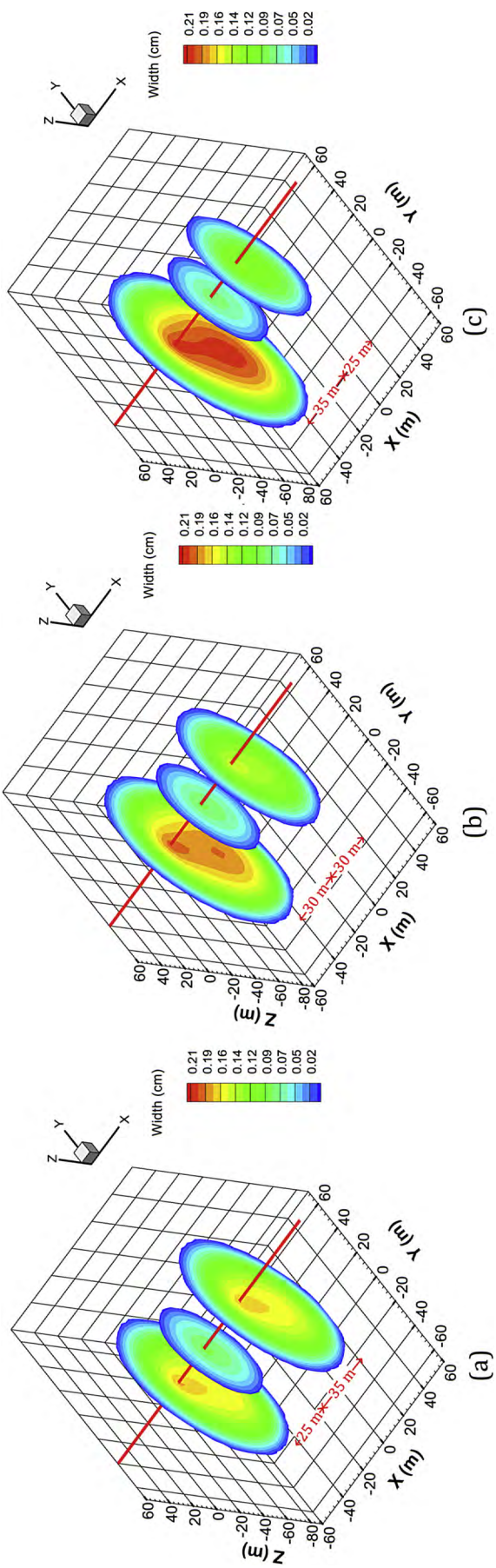

Fig. 17. Fracture geometry with consideration of well friction (a) Uneven spacing with S = 25 m between Frac 1 and Frac 2, S = 35 m between Frac 2 and Frac 3 (b) Equally spacing with S = 30 m (c) Uneven spacing with S = 35 m between Frac 1 and Frac 2, S = 25 m between Frac 2 and Frac 3.

fractures, which is another typical fracture geometry encountered in hydraulic fracturing, will grow. A case with PKN shaped fractures is compared with previous radial fracture cases to reveal the role of fracture geometry in simultaneous fracture propagation.

Flow rate partitioning and fracture surface area evolution are compared between these two scenarios (Fig. 15). After the end of radial propagation, the middle fracture is under stronger compression in the PKN case. The inner fracture of the PKN shape receives smaller flow rate compared to the radial fracture and finally no fluid can enter it. Meanwhile, the fracture surface area of the PKN outer fracture gradually decreases below the area delivered by radial cases and the inner fracture area in PKN case is quite similar. These trends can be explained that, at early time, fractures are growing radially in both stress states, and thus similar flow rates and surface areas are observed. Once the stress barrier is reached in the PKN case, the growth ability of the fracture is impaired in the vertical direction and fracture widths start to dilate in the perforation layer. This also explains why outer fracture widths of the PKN fracture are larger as shown in Fig. 14. For the same reason, with the same injection volume, the PKN shape fractures expand into a smaller area than radial fractures which have less resistance to propagation (Fig. 15(a)). Also, since fracture aperture around the injection point of the PKN fracture is larger, the center fracture will endure more compression from outer fractures which results in more severe unbalanced distribution of flow rate among fractures (Fig. 15(b)). This is clearer when looking at the stress distribution. The normal stress distribution at the depth of the horizontal well is calculated with DDM (Fig. 16). The width of each fracture, enlarged with a same constant, is also drawn. In the PKN case, higher compressive stress is observed, which results in a stronger contrast between outer and inner fracture width and length.

When well friction is considered, the larger the distance between the fracture and the heel of the well, the greater the pressure friction loss. As a result, the fracture close to the injection point will gain most of the pumped fluid. At early stages, when the stress shadowing effect is not significant, the fracture closest to the toe of the well develops slowly due to the friction loss of pressure. As the fracture grows, the compression from outer fractures starts to restrict the propagation of the middle fracture, which gradually becomes the smallest fracture in this stage. If friction exists in the wellbore, the optimized perforation spacing may vary. Based on the above analysis, suppressing the propagation of fractures close to injection might help other fractures receive more fluid (Fig. 17). Consequently, moving the inner fracture closer to the heel of the well could help balance fracture growth within the three fracture stage (Fig. 17(a)). Moving to the opposite direction (Fig. 17(c)), however, will exaggerate the difference among the fractures.

4.3. The impact of thermal effects on hydraulic fracturing

This section aims at investigating the sensitivity of fracture propagation to fluid viscosity changes caused by temperature redistribution. Fluid viscosity is important in the sense that fracture geometry can be a function of fluid rheology. The distance of proppant travelling and proppant settlement are also strongly affected by fluid viscosity.

A general exponential law is used here to characterize the

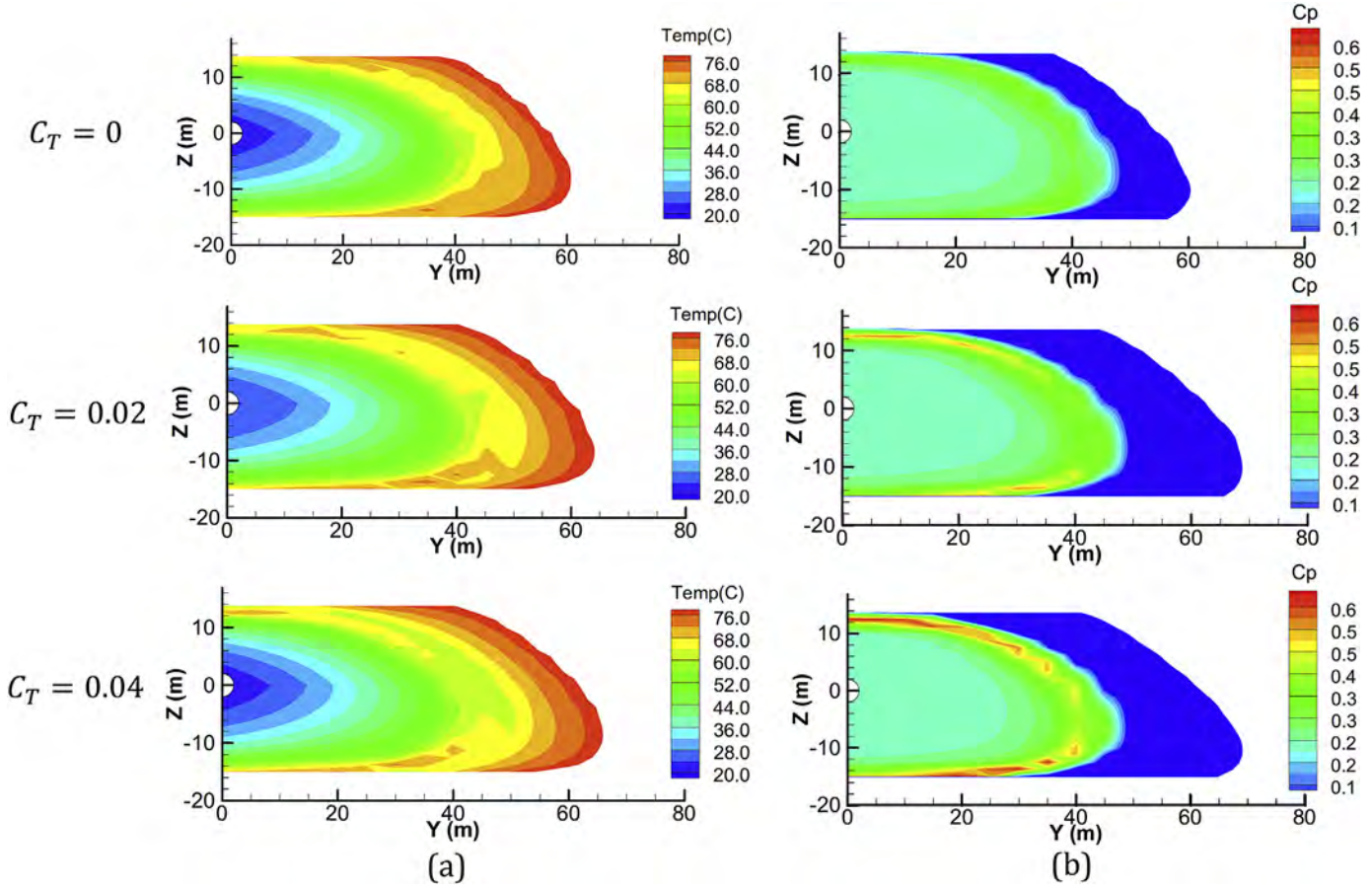

Fig. 18. Temperature (a) and proppant volume fraction (b) distribution at the end of injection with different temperature coefficient.

relation between viscosity and fluid temperature.

$$\mu(T) = \mu_0 \exp(-C_T(T - T_0)) \tag{31}$$

where μ is fluid component viscosity, T is temperature, C_T is temperature coefficient and subscript 0 represents reference conditions. A single fracture with two stage injections is modeled. At the first stage, base fluid is injected with a rate 20 bbl/min for 2.5 min. In the following stage, proppant with properties in Table 4 is pumped in with Gel for another 10 min. Then, the well is shut-in and the last calculation time step is 16 min after injection stops. Three cases are designed with different temperature coefficients, which are 0, 0.02 and 0.04 (1/°C) respectively. Injection fluid temperature and reservoir initial temperature are listed in Table 4. The maximum proppant concentration is chosen to be 0.6.

Cool fracturing fluid injected into high temperature rock mass is heated by heat exchange in the well bore and heat exchange through the fracture walls. Temperature distribution at the end of injection is shown in Fig. 18. The increase of temperature results in fluid viscosity loss which affects fracture geometries and proppant distributions. The decrease of viscosity enhances fracture propagation in length however imparts the dilation of fracture aperture. According to Eq. (30), fracture radius is inversely proportional to 1/9 of fluid viscosity while proppant settling velocity is inversely proportional to 0.43 of the viscosity. Thus proppant settlement is more sensitive to fluid viscosity change than fracture propagation. Though fracture can propagate faster with smaller viscosity, the quick settlement of proppants limits the proppant travel distance and proppant bridging happens earlier in the case with more viscosity loss (Fig. 18(b)). Moreover, the fluid closest to the fracture tip has the highest temperature (Fig. 18(a)) since this portion of fluid has been heated for the longest time after being injected into fractures. The fluid viscosity at fracture front, therefore, has the most significant loss, which further strengthens the bridging effect at fracture tip.

During the shut-in period, the fracturing fluid leaks off into the reservoir rock, which decreases the net pressure within the fractures. Fracture width shrinkage resulting from pressure loss would prohibit the transport of proppant, and when the maximum allowable concentration is reached, proppants pack together and stars acting as immobile porous media. Greater viscosity can help prevent proppant bridging as well as proppant settling as shown in Fig. 19. For the case without thermal effects, a more uniform distribution of proppant after shut-in is observed, which is able to maintain higher fracture conductivity during production. The study of fluid thermal effects aids in deciding the type of fluid to be used for a specific reservoir and predicting the proppant distribution under different conditions.

Besides the sensitivity of fluid viscosity to temperature, other fluid properties can also be affected by temperature changes. With the model introduced in this paper, it's possible to evaluate the impact of fluid property changes on fracturing effectiveness, such as fracture size and propped fracture area, which provides a more comprehensive understanding of the fracturing process.

5. Conclusions

A fully thermal-hydro-mechanical coupled numerical model

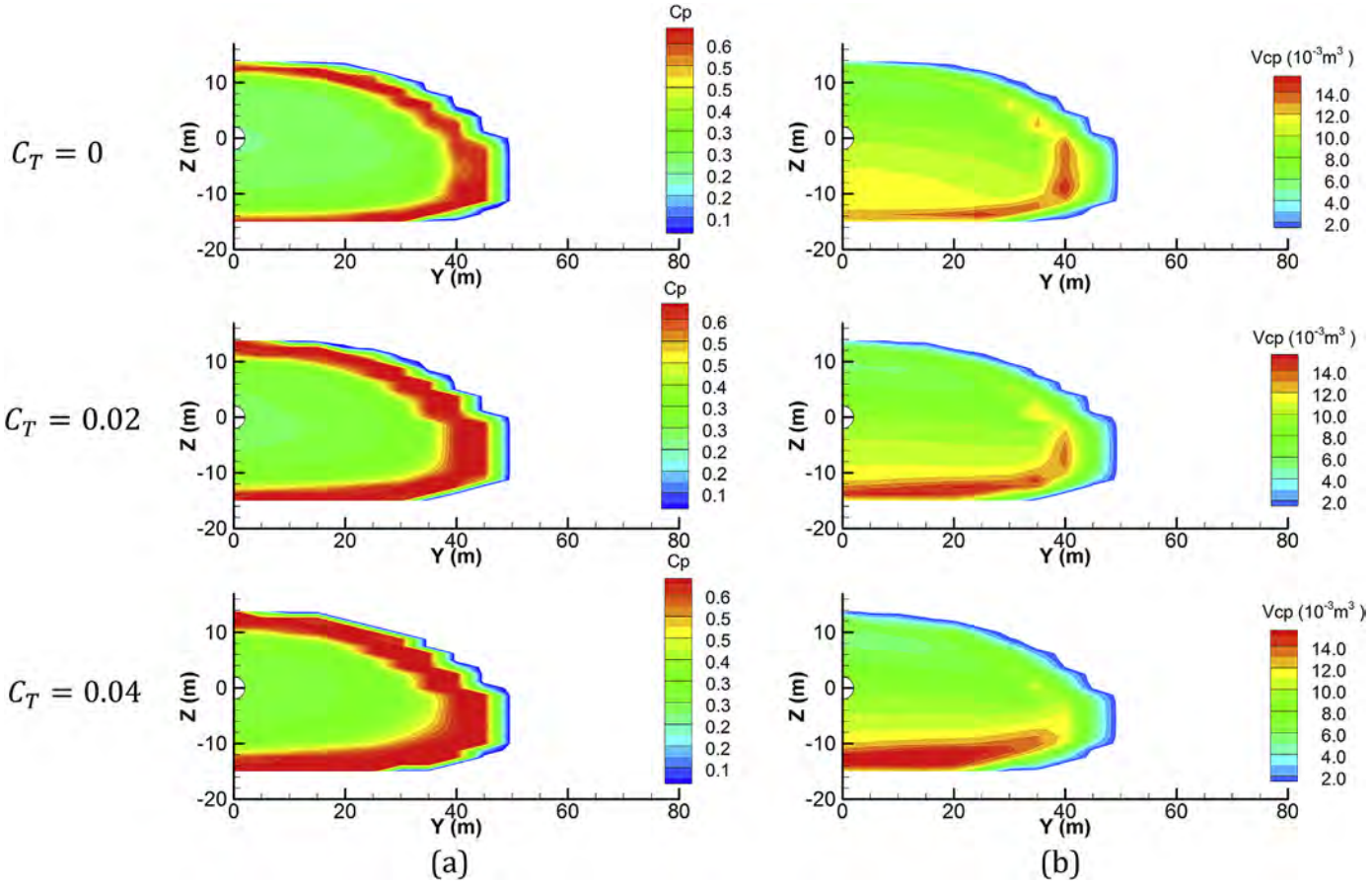

Fig. 19. Proppant concentration (a) and proppant volume (b) distribution after injection stops for 16 min.

which integrates wellbore and fracture parts is introduced in this paper. This model is able to simulate fracture height growth in heterogeneous formations, simultaneous propagation of multiple fractures, and proppant transport and settling with the consideration of thermal effects. Based on the modeling results, several conclusions can be drawn:

- The in-situ stress state is critical for fracture configurations. A good knowledge of the stress states is required to deliver reliable results.
- The stress shadow effect does not only affect the configurations of fractures, but also influence the proppant distribution among fractures. Early proppant brigding may happen in inner fractures which further prohibits the fracture propagation.
- The strength of the stress shadow effect is related to fracture geometries. With the same spacing, the PKN shaped outer fracture apply stronger compression to the inner fractures than radial fractures. Hence, the optimization of fracture spacing should also consider the effect of fracture shapes.
- When well friction exists, the optimal fracture placement will change. More fractures should be placed close to the heel of the well to partially compensate the pressure loss along the wellbore.
- The change of fluid viscosity with temperature affects the model in two ways. The heated fluid with lower viscosity tends to drive longer but thinner fractures, which facilitates the formation of proppant bridges. The proppant placement during the shut-in period is also affected by fluid viscosity, and the lower the fluid viscosity the faster the proppants will settle. Because of the importance of the propped fracture surface area, it is necessary to correctly model both the fracture behaviors and the proppant movement.

Acknowledgement

This project is supported by the National Natural Science Foundation of China (Grant number: 51674010). H. Tang thanks K. P. Cheong for his technical support, and Dr. H. Li, Dr. Y. Zhang, Kang Wang and Kevin L. McCormack for their insightful suggestions on this work.

References

Abbas, S., Lecampion, B., Prioul, R., 2013. Competition between transverse and axial hydraulic fractures in horizontal wells. In: SPE Hydraulic Fracturing Technology Conference. Society of Petroleum Engineers.

Adachi, J., Siebrits, E., Peirce, A., Desroches, J., 2007. Computer simulation of hydraulic fractures. Int. J. Rock Mech. Min. Sci. 44, 739–757. http://dx.doi.org/10.1016/j.ijrmms.2006.11.006.

Barree, R.D., 1983. A practical numerical simulator for three-dimensional fracture propagation in heterogeneous media. In: SPE Reservoir Simulation Symposium. Society of Petroleum Engineers.

Behnia, M., Goshtasbi, K., Zhang, G., Mirzeinaly Yazdi, S.H., 2015. Numerical modeling of hydraulic fracture propagation and reorientation. Eur. J. Environ. Civ. Eng. 19, 152–167.

Bunger, A.P., Zhang, X., Jeffrey, R.G., 2012. Parameters affecting the interaction among closely spaced hydraulic fractures. Spe J. 17, 292–306. http://dx.doi.org/10.2118/140426-pa.

Chen, N.H., 1979. An explicit equation for friction factor in pipe. Ind. Eng. Chem. Fundam. 18, 296–297. http://dx.doi.org/10.1021/i160071a019.

Cheng, Y., 2012a. Impacts of the number of perforation clusters and cluster spacing on production performance of horizontal shale-gas wells. SPE Reserv. Eval. Eng. 15, 31–40. http://dx.doi.org/10.2118/138843-PA.

Cheng, Y., 2012b. Mechanical interaction of multiple fractures-exploring impacts of the selection of the spacing/number of perforation clusters on horizontal shale-gas wells. Spe J. 17, 992–1001. http://dx.doi.org/10.2118/125769-PA.

Cipolla, C.L., Lolon, E., Mayerhofer, M.J., Warpinski, N.R., 2009. The effect of proppant distribution and un-propped fracture conductivity on well performance in unconventional gas reservoirs. In: SPE Hydraulic Fracturing Technology Conference. Society of Petroleum Engineers.

Cohen, C.E., Weng, X., Kresse, O., 2013. Influence of fracturing fluid and reservoir temperature on production for complex hydraulic fracture network in shale gas reservoir. Soc. Pet. Eng. - Asia Pac. Unconv. Resour. Conf. Exhib. 2013 Deliv. Abund. Energy a Sustain. Futur. 2, 922–941.

Colebrook, C.F., White, C.M., 1937. Experiments with fluid friction in roughened pipes. Proc. R. Soc. Lond. A. Math. Phys. Sci. 367–381.

Crouch, S.L., 1976. Solution of plane elasticity problems by the displacement discontinuity method. I. Infinite body solution. Int. J. Numer. Methods Eng. 10, 301–343.

Eckhardt, B., Schneider, T.M., Hof, B., Westerweel, J., 2007. Turbulence transition in pipe flow. Annu. Rev. Fluid Mech. 39, 447–468. http://dx.doi.org/10.1146/annurev.fluid.39.050905.110308.

Economides, M.J., Nolte, K.G., 2000. Reservoir Stimulation. Wiley Chichester.

Fisher, M.K., Warpinski, N.R., 2012. Hydraulic-fracture-height growth: real data. SPE Prod. Oper. 27, 8–19.

Friehauf, K.E., 2009. Simulation and Design of Energized Hydraulic Fractures.

Fu, P., Johnson, S.M., Carrigan, C.R., 2013. An explicitly coupled hydro-geomechanical model for simulating hydraulic fracturing in arbitrary discrete fracture networks. Int. J. Numer. Anal. Methods Geomech. 37, 2278–2300. http://dx.doi.org/10.1002/nag.2135.

Geertsma, J., De Klerk, F., 1969. A rapid method of predicting width and extent of hydraulically induced fractures. J. Pet. Technol. 21, 1–571. http://dx.doi.org/10.2118/2458-PA.

Grunberg, L., Nissan, A.H., 1949. The energies of vaporisation, viscosity and cohesion and the structure of liquids. Trans. Faraday Soc. 45, 125–137.

Gupta, P., Duarte, C.A., 2014. Simulation of non-planar three-dimensional hydraulic fracture propagation. Int. J. Numer. Anal. Methods Geomech. 38, 1397–1430. http://dx.doi.org/10.1002/nag.2305.

Haddad, M., Du, J., Vidal-Gilbert, S., 2016. Integration of dynamic microseismic data with a true 3D modeling of hydraulic fracture propagation in vaca muerta shale. SPE Hydraul. Fract. Technol. Conf. http://dx.doi.org/10.2118/179164-MS.

Heister, T., Wheeler, M.F., Wick, T., 2015. A primal-dual active set method and predictor-corrector mesh adaptivity for computing fracture propagation using a phase-field approach. Comput. Methods Appl. Mech. Eng. 290, 466–495.

Howard, G.C., Fast, C.R., 1957. Optimum fluid characteristics for fracture extension. In: Drilling and Production Practice. American Petroleum Institute.

Lecampion, B., Desroches, J., 2015. Simultaneous initiation and growth of multiple radial hydraulic fractures from a horizontal wellbore. J. Mech. Phys. Solids 82, 235–258. http://dx.doi.org/10.1016/j.jmps.2015.05.010.

Maccaferri, F., Bonafede, M., Rivalta, E., 2011. A quantitative study of the mechanisms governing dike propagation, dike arrest and sill formation. J. Volcanol. Geotherm. Res. 208, 39–50. http://dx.doi.org/10.1016/j.jvolgeores.2011.09.001.

Maerten, F., Maerten, L., Pollard, D.D., 2014. IBem3D, a three-dimensional iterative boundary element method using angular dislocations for modeling geologic structures. Comput. Geosci. http://dx.doi.org/10.1016/j.cageo.2014.06.007.

Mastrojannis, E.N., Keer, L.M., Mura, T., 1979. Stress intensity factor for a plane crack under normal pressure. Int. J. Fract. 15, 247–258.

McClure, M., Babazadeh, M., Shiozawa, S., Huang, J., 2015. Fully coupled hydromechanical simulation of hydraulic fracturing in three-dimensional discrete fracture networks. In: SPE Hydraulic Fracturing Technology Conference. Society of Petroleum Engineers.

McClure, M., Horne, R.N., 2013. Discrete Fracture Network Modeling of Hydraulic Stimulation: Coupling Flow and Geomechanics. Springer Science & Business Media.

McClure, M.W., Horne, R.N., 2014. An investigation of stimulation mechanisms in Enhanced Geothermal Systems. Int. J. Rock Mech. Min. Sci. 72, 242–260.

Miller, C., Waters, G., Rylander, E., 2011. Evaluation of production log data from horizontal wells drilled in organic shales. North Am. Unconv. Gas. Conf. Exhib. SPE 144326. http://dx.doi.org/10.2118/144326-ms.

Nicodemo, L., Nicolais, L., Landel, R.F., 1974. Shear rate dependent viscosity of suspensions in newtonian and non-newtonian liquids. Chem. Eng. Sci. 29, 729–735. http://dx.doi.org/10.1016/0009-2509(74)80189-2.

Okada, Y., 1985. Surface deformation due to shear and tensile faults in a half-space. Int. J. Rock Mech. Min. Sci. Geomech. Abstr. 75, 1135–1154. http://dx.doi.org/10.1016/0148-9062(86)90674-1.

Olson, J.E., 1991. Fracture mechanics analysis of joints and veins. PhD Dissertation. Stanford University.

Peaceman, D.W., 1978. Interpretation of well-block pressures in numerical reservoir simulation. Soc. Pet. Eng. J. 18, 183–194. http://dx.doi.org/10.2118/6893-PA.

Peirce, A., Bunger, A., 2013. Interference fracturing: non-uniform distributions of perforation clusters that promote simultaneous growth of multiple hydraulic fractures. SPE J. 20, 384–395. http://dx.doi.org/10.2118/172500-PA.

Reyes, J.S., Hutchins, R.D., Parris, M.D., Corporation, S.T., 2014. Experimental Determination of the Effect of Pressure on Fluid Loss for Several Fracturing Fluids. SPE Int.

Ribeiro, L., 2013. Development of a Three-dimensional Compositional Hydraulic Fracturing Simulator for Energized Fluids.

Ribeiro, L.H., Sharma, M.M., 2013. A new 3D compositional model for hydraulic fracturing with energized fluids. SPE Prod. Oper. SPE159812 259–267. http://dx.doi.org/10.2118/115750-PA.

Ritz, E., Mutlu, O., Pollard, D.D., 2012. Integrating complementarity into the 2D displacement discontinuity boundary element method to model faults and fractures with frictional contact properties. Comput. Geosci. 45, 304–312. http://dx.doi.org/10.1016/j.cageo.2011.11.017.

Sesetty, V., Ghassemi, A., 2015. A numerical study of sequential and simultaneous

hydraulic fracturing in single and multi-lateral horizontal wells. J. Pet. Sci. Eng. 132, 65–76. http://dx.doi.org/10.1016/j.petrol.2015.04.020.
Sheibani, F., 2013. Solving Three Dimensional Problems in Natural and Hydraulic Fracture Development: Insight from Displacement Discontinuity Modeling.
Shiozawa, S., McClure, M., 2016. Simulation of proppant transport with gravitational settling and fracture closure in a three-dimensional hydraulic fracturing simulator. J. Pet. Sci. Eng. 138, 298–314. http://dx.doi.org/10.1016/j.petrol.2016.01.002.
Sneddon, I.N., 1946. The distribution of stress in the neighbourhood of a flat elliptical crack in an elastic solid. Proc. R. Soc. Lond. A-187, 229–260. http://dx.doi.org/10.1017/S0305004100025585.
Taleghani, A., Dahi Taleghani, A., 2009. Analysis of Hydraulic Fracture Propagation in Fractured Reservoirs: an Improved Model for the Interaction between Induced and Natural Fractures. http://dx.doi.org/10.5829/idosi.wasj.2013.28.11.2005. PhD Thesis, UT.
Tao, Q., Ghassemi, A.A., 2010. Simulation of fluid flow in a naturally fractured poro-thermoelastic reservoir. In: 44th US Rock Mechanics Symposium and 5th US-Canada Rock Mechanics Symposium. American Rock Mechanics Association.
Timoshenko, S., Goodier, J.N., 1951. Theory of elasticity. J. Elast. http://dx.doi.org/10.1007/BF00046464.
Valkó, P., Economides, M.J., 1995. Hydraulic Fracture Mechanics. Wiley, New York.
Valkó, P.P., Lee, W.J., 2010. A better way to forecast production from unconventional gas wells. SPE Annu. Tech. Conf. Exhib. SPE 134231. http://dx.doi.org/10.2118/134231-MS.
Weng, X., Kresse, O., Cohen, C.-E., Wu, R., Gu, H., 2011. Modeling of hydraulic-fracture-network propagation in a naturally fractured formation. SPE Prod. Oper. 26, 368–380. http://dx.doi.org/10.2118/140253-PA.
Wu, K., 2014. Numerical Modeling of Complex Hydraulic Fracture Development in Unconventional Reservoirs.
Wu, K., Olson, J.E., 2015. Simultaneous multifracture treatments: fully coupled fluid flow and fracture mechanics for horizontal wells. SPE J. 20, 337–346. http://dx.doi.org/10.2118/167626-PA.
Zhang, X., Jeffrey, R.G., Thiercelin, M., 2009. Mechanics of fluid-driven fracture growth in naturally fractured reservoirs with simple network geometries. J. Geophys. Res. Solid Earth 114.
Zhang, X., Jeffrey, R.G., Thiercelin, M., 2007. Deflection and propagation of fluid-driven fractures at frictional bedding interfaces: a numerical investigation. J. Struct. Geol. 29, 396–410.